University of BRISTOL

Peer reviewed version

Probing the deep critical zone beneath the Luquillo Experimental Forest, Puerto Rico

1 *Revised submission for the special issue of ESPL on deep CZ*

2

Probing the deep critical zone beneath the Luquillo Experimental

Forest, Puerto Rico

5

6 [1,*]Buss H.L., [2]Brantley S.L., [3]Scatena F.N., [2]Bazilievskaya E.A., [4]Blum A., [5]Schulz

7 M., [3]Jiménez R., [5]White A.F., [6]Rother G., [7]Cole D.

8

[1]School of Earth Sciences, University of Bristol, Wills Memorial Building, Bristol BS8
    1RJ, UK
[2]Earth and Environmental Systems Institute, The Pennsylvania State University,
    University Park, PA, 16802, USA
[3]Department of Earth and Environmental Sciences, University of Pennsylvania, 230
    S 33rd Street, Philadelphia, PA 19104, USA
[4]U.S. Geological Survey, 3215 Marine Street, Boulder, CO 80303, USA
[5]U.S. Geological Survey, 345 Middlefield Road, MS 420, Menlo Park, CA 94025,
    USA
[6]Chemical Sciences Division, Oak Ridge National Laboratory, Oak Ridge, TN 37831,
    USA
[7]School of Earth Sciences, Ohio State University, Columbus, OH 43210 USA

*Corresponding author: h.buss@bristol.ac.uk

23

24 20 January 2013

25

26 Short Title: Luquillo deep critical zone

28

Abstract

29

30   Recent work has suggested that weathering processes occurring in the

31   subsurface produce the majority of silicate weathering products discharged to the

32   world's oceans, thereby exerting a primary control on global temperature via the

33   well-known positive feedback between silicate weathering and CO_2. In addition,

34   chemical and physical weathering processes deep within the *critical zone* create

35   aquifers and control groundwater chemistry, watershed geometry and regolith

36   formation rates. Despite this, most weathering studies are restricted to the shallow

37   critical zone (e.g., soils, outcrops). Here we investigate the chemical weathering,

38   fracturing and geomorphology of the deep critical zone in the Bisley watershed in the

39   Luquillo Critical Zone Observatory, Puerto Rico, from two boreholes drilled to 37.2

40   and 27.0 m depth, from which continuous core samples were taken. Corestones

41   exposed aboveground were also sampled. Weathered rinds developed on exposed

42   corestones and along fracture surfaces on subsurface rocks slough off of exposed

43   corestones once rinds attain a thickness up to ~1 cm, preventing the corestones

44   from rounding due to diffusion limitation. Such corestones at the land surface are

45   assumed to be what remains after exhumation of similar, fractured bedrock pieces

46   that were observed in the drilled cores between thick layers of regolith. Some of

47   these subsurface corestones are massive and others are highly fractured, whereas

48   aboveground corestones are generally massive with little to no apparent fracturing.

49   Subsurface corestones are larger and less fractured in the borehole drilled on a road

50   where it crosses a ridge compared to the borehole drilled where the road crosses the

51   stream channel. Both borehole profiles indicate that the weathering zone extends to

52   well below the stream channel in this upland catchment; hence weathering depth is

1

53 not controlled by the stream level within the catchment and not all of the water in the

54 watershed is discharged to the stream.

55

Introduction

56

57   Weathering of bedrock is the initial step in the soil-forming process and the

58 primary contributor of solutes and sediments to the hydrosphere. However, the

59 interfaces where intact bedrock weathers to disaggregated material (e.g., corestones

60 and saprolite) are often hidden deep within the critical zone. The vast majority of

61 weathering studies in the natural environment focus on the shallow critical zone:

62 soils, sediments, regolith, saprolite, and outcrops within several meters of the land

63 surface. Although weathering processes have been quantified in these surficial

64 zones, it is likely that weathering of primary minerals along bedrock fractures located

65 in the groundwater or deeper vadose zones supplies significant weathering products

66 to streams and oceans (Anderson and Dietrich, 2001; Calmels et al., 2011; Kurtz et

67 al., 2011; Tipper et al., 2006a; Tipper et al., 2006b). These observations may be

68 particularly important in the tropics, where weathering forms saprolites tens or even

69 hundreds of meters thick (Ollier and Pain, 1996). Weathered materials from such

70 depths are extremely difficult to retrieve and are thus rarely studied.

71   Many models of weathering and landscape evolution rely on assumptions of

72 steady state regolith thickness wherein the rates of bedrock weathering and physical

73 erosion are assumed to be equal. Only a few studies have tested this assumption by

74 comparing erosion rates measured by cosmogenic isotopes to regolith production

75 rates measured by U-Th disequilibria (e.g., Dosseto et al., 2012; Dosseto et al.,

76 2008). Furthermore, only a few researchers have proposed feedbacks that might

2

77 control such coupling (e.g., Fletcher et al., 2006; Riebe et al., 2004; West et al.,

78 2005). A further complication is that some researchers consider such steady-state

79 assumptions to only be applicable to the "mobile soil" that moves down hillslopes

80 (Dietrich et al., 1995; Heimsath et al., 1997) while others assume steady state for the

81 entire soil + saprolite + incipiently weathered rock zone (e.g., Fletcher et al., 2006;

82 White, 2002). In the former case, erosion and weathering advance might be coupled

83 only over a few tens of centimeters while in the latter case the two processes might

84 be coupled to tens of meters. A few researchers have suggested that biota may act

85 to couple surface erosion to the production of weathered material in the "mobile soil"

86 layer (e.g., Roering et al., 2010). Alternatively, Fletcher and others suggested that

87 pore water chemistry and weathering particle size distributions might couple surficial

88 erosion to weathering advance even to hundreds of meters depth (Brantley et al.,

89 2011; Fletcher and Brantley, 2010; Fletcher et al., 2006). Nonetheless, no fully

90 coupled model has been proposed for either shallow "mobile soil" or deeper regolith

91 systems.

92   In contrast, an apparent *de*coupling of deep and surficial nutrient cycles has

93 been noted in the tropics and subtropics due to isolation of ecosystems by highly

94 weathered, deep (~10's to 100's of m) regoliths of, which are typically depleted in

95 base cations and mineral nutrients such as Ca, Mg, and P (e.g., Bruijnzeel, 1991).

96 For example, in the Luquillo Critical Zone Observatory (LCZO) in northeastern

97 Puerto Rico (Figure 1), thick regolith blankets the landscape. At ridge tops, where

98 hydrologic flow from the surface to the deep regolith is effectively 1-D, this thick,

99 nutrient-poor regolith effectively isolates microbial communities at depth from the

100 ecosystems at the surface, as evidenced by depth profiles of solid and solute organic

3

101 carbon, mineral nutrients, and microbial cell densities (e.g., Murphy, 1995; White et

102 al., 1998; Buss et al., 2005; Buss et al., 2010a,b).

103   In addition to ecological decoupling, chemical weathering in the humid tropics

104 may also be decoupled by thick, highly leached regolith, such that chemical export

105 budgets are dominated by weathering along fractures in the subsurface. Therefore,

106 the density, spacing, connectivity, and transmissivity of bedrock fractures and the

107 groundwater residence time may exert significant control on chemical weathering

108 fluxes out of watersheds. In the granitic Rio Icacos watershed of the LCZO, Si/Ge

109 ratios and Si isotopes indicate that mineral weathering reactions that occur only at

110 the bedrock-saprolite interface (plagioclase and amphibole dissolution) are the

111 dominant source of the dissolved Si to the river during baseflow (Kurtz et al., 2011;

112 Lugolobi et al., 2010; Ziegler et al., 2005). Kurtz et al. (2011) also showed that the

113 rising limbs of storm hydrographs in the Rio Icacos were dominated by groundwater,

114 coinciding with a pulse of solutes from fracture-sourced weathering reactions. As the

115 storms progressed, the hydrologic flux became dominated by more dilute water

116 sources: rainwater and surficial runoff, finally returning to groundwater-dominated

117 flow as the hydrograph returned to baseflow conditions after several hours.

118   Given the expense and difficulty of sampling deep (10's to 100's of m; i.e,

119 below the hand-augerable regolith) into the critical zone, it is common that

120 investigators make extrapolations or inferences about weathering processes at

121 depth. It is rare that drilling can accompany a weathering study to test these

122 inferences. Furthermore, well drilling typically does not include continuous core

123 sampling, especially within highly fractured and partially weathered rock, which is

124 technically difficult to accomplish. In this contribution, we report the first results of

125 drilling in one of the watersheds under study within the LCZO: Bisley. In that

4

126   watershed, one of the notable weathering features are angular boulders that have

127   been exposed at the land surface (Fletcher and Brantley, 2010; Pike et al., 2010).

128   Both of those studies noted that, on average, the size of the largest of these

129   boulders at any location decreases upward as elevation increases (see schematic

130   shown in Figure 2). Although some boulders may have been transported, this is not

131   expected to have altered the general relationship between the size of the largest

132   boulders and elevation. Fletcher and Brantley mapped these boulders throughout the

133   Bisley watershed whereas Pike et al. measured sediment sizes in the river beds.

134   Based on these boulders, a series of hypotheses were made about the subsurface

135   and we test those hypotheses here.

136   Specifically, Fletcher and Brantley (2010) proposed that the changing size of

137   boulders is due to a previous regime of weathering (Stage 1 in Figure 2) that is now

138   being incised by the Bisley stream (Stage 2, Fig. 2, also see Figure 3). A longitudinal

139   profile of the Bisley I channel is shown in Figure 3 (Fletcher and Brantley, 2010),

140   which extends from the headwaters, past the Bisley I outlet (260 masl), and

141   continues along the main stem of the Bisley tributary (Bisley tributaries I and II join

142   the larger Bisley III). Just above 50 masl, the combined Bisley tributary joins the

143   main stem of the Rio Mameyes, where the river is bedrock-lined. Within the Bisley I

144   watershed, the size of the boulders at the land surface decreases upward with

145   elevation *only above ~200 masl* (below 200 masl, boulder size was invariant).

146   Fletcher and Brantley inferred that these boulders were formed in the subsurface as

147   water infiltrated into fractured rock; after weathering, the rocks became smaller with

148   time to form angular "corestones." By fitting a model for corestone development

149   during weathering to the size-elevation data, they inferred that the range in elevation

150   over which corestones vary in size – ~200 m – corresponds to a ~135 meter-thick

5

151 weathering layer that today contains angular boulders surrounded by saprolite.

152 Beneath this 135 meter-thick layer, they hypothesized that bedrock was still fractured

153 but insignificantly weathered– they termed this the weathering, or corestone,

154 baseline. Corestones of roughly the same size (due to equal fracture spacing) were

155 assumed to emerge from this baseline at 135 m depth. As corestones interacted

156 with infiltrating fluids, they became smaller with time. The model is consistent with a

157 depth to the corestone baseline of ~100 m at the uppermost ridge of the Bisley I

158 catchment and ~30 m at the outlet of Bisley I. The gradient of the corestone baseline

159 was inferred to be identical to the Bisley stream above its confluence with the

160 Mameyes. Thus, the Bisley stream was assumed to be eroding into an already

161 weathered layer of saprolite+corestones. While the authors argued that the deep

162 weathering had been previously imposed on the system, they pointed out that it is

163 also possible that the deep weathering is ongoing today such that weathering and

164 erosion are coupled to depths possibly exceeding 100 m.

165   The model just summarized is not well constrained by data other than

166 observations of corestone size at land surface. Nonetheless, other researchers have

167 made similar estimates of depth to un-weathered bedrock (Schellekens et al., 2004).

168 Here, we report results from drilling at the mouth of the Bisley I catchment (260 masl)

169 where we tried to drill to the un-weathered bedrock to gain insight into how

170 subsurface CZ processes influence the structure, character, and properties of the

171 more readily observable, surficial CZ. We hypothesized that the corestone-

172 containing zone would terminate in fractured bedrock at about 30 m depth (230

173 masl), based on Fig. 3 in Fletcher and Brantley (2010) and Fig. 4 in Schellekens et

174 al. (2004). Furthermore, since smaller corestones exposed at the land surface at

175 higher elevations are presumed to have weathered for longer than larger corestones

6

176   at lower elevations, we also hypothesized that weathering rinds on large and small

177   corestones (at low and high elevations, respectively) would differ. To investigate that

178   inference, we also present chemical evidence identifying the weathering reactions

179   within the saprolite and within the weathering rinds on the angular corestones.

180

181   **Field Setting**

182   The Luquillo Mountains in northeastern Puerto Rico are characterized by

183   steep, rugged slopes, highly dissected valleys, a hot and humid climate, and dense,

184   tropical vegetation that grows over deep, highly weathered saprolites. The Luquillo

185   Mountains host the 113-km^2 Luquillo Experimental Forest (LEF), a research

186   preserve administered by the U.S. Forest Service that has been designated a critical

187   zone observatory (CZO) by the National Science Foundation. Several large river

188   systems drain the LEF north to the Atlantic Ocean (Rio Mameyes, Rio Sabana, Rio

189   Espiritu Santo, and Rio Fajardo) or south to the Caribbean Sea (Rio Blanco).

190   The Bisley experimental watersheds are a sequence of adjacent catchments

191   (numbered 1-5, from east to west) that drain into the Rio Mameyes (Figure 1).

192   Elevation in the 44 km^2 (17.8 km^2 gaged area) Rio Mameyes watershed ranges from

193   80 to 1050 masl. The Bisley watersheds are covered by mature Tabonuco type

194   forest and have elevation that ranges from 260-400 masl and drainages from 6-50

195   ha in area (Scatena, 1989). The climate is humid, subtropical and has precipitation in

196   every month. Mean monthly temperatures average about 24° C in the winter and

197   about 27.5° C in the summer (Schellekens et al., 2004; National Weather Service,

198   2007). Rainfall increases with altitude in the Luquillo Mountains, from about 2,500 to

199   4,500 mm y^{-1} over 1,200 m of elevation (Garcia-Martino et al., 1996). The Bisley

7

200   watersheds experienced an average rainfall of 3482 mm y^{-1} between 1988 and 2003

201   (Heartsill-Scalley et al., 2007). Surface hydrology is characterized by intense rainfall

202   and rapid streamflow response that is dominated by fast, near-surface flow paths

203   (Schellekens et al., 2004).

204   The Bisley watersheds are underlain by bedrock of the ~100 Ma, basaltic to

205   andesitic, marine-bedded, volcaniclastic Fajardo formation (Jolly et al., 1998). This

206   formation developed from a near-sea level volcanic complex that produced

207   pyroclastic debris that was deposited in a shallow marine environment after transport

208   and re-working (Seiders, 1971). The Fajardo formation likely underwent weak

209   contact metamorphism during the intrusion of the nearby Rio Blanco quartz diorite

210   stock 49-42 Ma (Smith et al., 1998). The Bisley catchments are underlain by an

211   upper thick-bedded tuff unit of the Fajardo formation which includes some breccias,

212   lithic andesitic clasts, calcareous siltstone, and some pumice and red scoria (Briggs

213   and Cortes-Aguilar, 1980).

214   Ridges in the Bisley watersheds are mantled by thick (> 9 m), highly cohesive

215   regolith (including soil, saprolite, and/or transported material). Ridgetop soils are

216   Ultisols of the Humatas Series, which are 0.8-1.0 m deep, moderately well-drained,

217   very-fine, parasesquic, isohyperthermic Typic Haplohumults (Scatena, 1989; Silver

218   et al., 1994; USDA NCRS, 2002). Hand-augered regolith cores to 9 m depth in the

219   valley and 16 m depth on the highest ridge revealed highly weathered saprolite

220   nearly devoid of primary minerals (Dosseto et al., 2012; Frizano et al., 2002).

221   Landslides, soil creep, and tree throws incise and sharpen the ridges, and

222   leave high-angle hillslopes with thinner regolith (typically 1 to 3 m deep). Most

223   slopes, lower-elevation ridges, and valleys are riddled with exposed corestones.

224   Stream gradients in and around the Bisley catchments are steep, and hillslopes are

8

225 generally convex-concave in form. Specifically, the upper slope segments are

226 convex-upward, whereas middle sections are typically straight. The lower slope

227 segments are usually concave-upward when they pass into first order valleys and

228 straight where they join the main channel. More than half of the catchment has

229 slopes greater than 45% (Scatena, 1989). On an aerial basis, the Bisley landscape is

230 comprised of 17% ridges, 18% valleys and 65% slopes (Scatena and Lugo, 1995).

231 Shallow earth movement, soil creep and tree fall are important geomorphic

232 processes and previous research has indicated strong interrelationships between

233 topographic position, landscape stability, and soil and forest development (Heartsill-

234 Scalley et al., 2010; Scatena and Lugo, 1995; Silver et al., 1994). In general, ridges

235 are the most stable landforms, have the oldest stands of vegetation, highest

236 biomass, and the most soil organic matter and acid-leached soils (Scatena and

237 Lugo, 1995).

238   To investigate the geometry of the Bisley subsurface, Schellekens et al. (2004)

239 used hand augering and geo-electric sounding along the Bisley II stream channel

240 (~150 m southwest of the Bisley I stream channel) and along the ridge that divides

241 the Bisley I and II catchments. Their results were interpreted to show a deep and

242 spatially continuous bedrock-saprolite interface that runs parallel to the elevation-

243 profile of the stream channel, but is not parallel to the overall surface

244 topography(Schellekens et al., 2004).

245

246 **Methods**

247 *Drilling and sample collection*

9

248   Exposures of in-place bedrock (as opposed to corestones) are rare in the

249   Bisley watersheds due to dense vegetation and thick regolith. Boulders, interpreted

250   as corestones either in place or transported only short distances, were sampled from

251   locations at 234 to 369 m elevation along the Bisley I stream bank using a hand-

252   held, gas powered paleomagnetic drill equipped with a diamond-encrusted coring

253   drill bit 2 cm in diameter. Cores varied from 2 to 20 cm in length. In every case,

254   angular corestones were exposed at the land surface and the cores were collected

255   approximately perpendicular to the exposed corestone surface. The size of the

256   corestone was also estimated. Each corestone was roughly measured in 3

257   dimensions with a measuring tape to ± 0.5 m and corestone size was estimated as

258   the cube root of the product of the 3 dimensions following our earlier methodology

259   (Fletcher and Brantley, 2010). Corestone sampling locations and descriptions are

260   given in Table 1. Several corestones exposed by landslides were also sampled using

261   a rock hammer (Tables 2-3).

262   In addition to the core-drilling of the exposed boulders, we also investigated

263   deep, un-exposed bedrock from two 9.6 cm diameter (HQ) boreholes drilled to 37.2

264   and 27.0 m depth (B1W1 and B1W2, respectively) along Road 915 (B1W1: N18

265   18.933 W65 44.748, B1W2: N18 18,958 W65 44.726, referenced to the NAD83

266   datum; Figure 1), near the Bisley I stream gage. Drilling was done by Geo Cim Inc.

267   (Guaynabo, Puerto Rico) with a hydraulic rotary drill with diamond-impregnated drill

268   bits, using only water from the Bisley I stream as drilling fluid. Continuous core

269   samples through coherent rock were taken during drilling using an HQ-wireline

270   barrel.

271

10

272 *Analyses*

273   Bulk solid-state chemical analysis was performed on pulverized and sieved

274 (150 μm) rock and saprock samples. Solid samples were digested by lithium

275 metaborate fusion and major and minor elements were determined by inductively

276 coupled plasma atomic emission spectrometry (ICP-AES) at the SGS Mineral

277 Laboratories, Ontario, Canada. Additional solid samples underwent a multi-acid

278 digest and analysis for ferrous iron by wet chemical methods (SGS Mineral

279 Laboratories, Ontario, Canada). The Chemical Index of Alteration (CIA) was

280 calculated from the bulk elemental chemistry (Nesbitt and Young, 1982):

281 $$CIA = 100 \frac{Al_2O_3}{Al_2O_3 + CaO + Na_2O + K_2O} \tag{1}$$

282 The CIA documents the loss of mobile base cations Ca, Na, and K relative to Al,

283 which is assumed to be relatively immobile. Values of the CIA increase with

284 increasing degree of weathering to a maximum of 100. Fresh rock is typically $\leq$ 50.

285   Powder X-ray diffraction was performed at the USGS (Boulder, CO), using a

286 Siemens D500 diffractometer. Quantitative mineral abundances were determined

287 from powder X-ray diffraction data using the computer program ROCKJOCK (Eberl,

288 2003) and compared to bulk chemical abundances using HandLens (Eberl, 2008).

289 Thin sections were prepared from rock, weathered rock fragments, and saprock

290 samples (Spectrum Petrographics, Vancouver, WA, USA). Thin sections were

291 examined using an optical petrographic microscope and a field-emission scanning

292 electron microscope (model Leo-982; Carl Zeiss SMT Inc., Peabody, MA) equipped

293 with an energy dispersive spectroscopy (EDS) detector. Samples were prepared for

294 SEM by vacuum coating with Au.

11

295   Hand-drilled core samples of corestones collected along the Bisley I stream

296   (Table 1) were cut lengthwise, perpendicular to the rind-rock interface, to prepare

297   0.15 mm thick petrographic thin sections (Tulsa Section Incorporated, Coweta,

298   Oklahoma, USA). Mineral composition and morphology were examined using an

299   optical petrographic microscope and a Hitachi SEM unit (model S-3500N) coupled

300   with a Princeton Garmon Tech EDS unit at the Materials Characterization Laboratory

301   (MCL), Penn State. The spatial chemical variability across the rock-rind boundary

302   were studied by measuring Si, Ca, Al, Ti, Fe, Na, and Mg along a ~10 mm transect

303   on four 2 mm thick sections across the rock–rind boundary. In addition, the

304   thicknesses of the weathering rinds were estimated using image-processing software

305   (ImageJ). Bulk chemical compositions were measured on the corestone samples by

306   carefully separating un-weathered rock from weathered rinds and analyzing them

307   separately ICP-AES, at MCL, Penn State.

308   Mass transfer coefficients, $\tau_{i,j}$, were calculated from the elemental transect

309   data collected on the corestone thin sections. "Tau" ratios concentrations of mobile

310   elements to concentrations of a relatively immobile element (here Al) to document

311   the mass transfer (loss or gain) of an element j relative to the parent rock

312   composition (Anderson et al., 2002; Brimhall and Dietrich, 1987). Here the deepest

313   analysis of each transect was used as the parent composition.

$$\tau_{Al,j} = \left(\frac{C_{j,w} C_{Al,p}}{C_{j,p} C_{Al,w}} \right) - 1 \tag{2}.$$

315   Here, $C_{j,w}$ is the mass fraction of element j in the weathered material, and $C_{j,p}$ is the

316   mass fraction of element j in the parent material. If $\tau_{Ti,j}$ = -1, element j is entirely lost.

317   If $\tau_{Ti,j}$ > 0, a net gain of element j relative to the parent rock is indicated.

12

318   Two corestones exposed at different elevations were sampled for neutron

319   scattering (NS) analysis: DR-4 and DR-7 (Table 5). Both samples consist of fine-

320   grained slightly metamorphosed volcaniclastic siltstone. These samples were chosen

321   for their similar texture (fine-grained) and rind thickness. Double-polished thick

322   sections were prepared from samples cut perpendicular to the core-rind interface

323   following methods in the literature (Jin et al., 2011). Under optical microscopy, the

324   cores of both samples were grey in color. In DR-7, the grey core grades into a tan-

325   colored zone followed by zones of white, then red. In DR-4, the grey core grades into

326   a brownish zone followed by zones of pink, then red. Under optical microscopy, grain

327   size within the rind of DR-4 is visibly larger and more variable than in the rind of DR-

328   7.

329   Small-angle neutron scattering (SANS) measurements were conducted on

330   beamline NG7 at the National Center for Neutron Research (NCNR) of the National

331   Institute of Standard and Technology (NIST, Gaithersburg, USA). Using a wave

332   length (λ) for neutrons of 8.09 Å, the scattered intensity was measured at sample to

333   detector distances of 1.0, 4.0, and 15.0 m using a 2D detector for neutrons with

334   different values of the scattering vector (Q). Thin sections were mounted behind a

335   cadmium plate with a 1 mm x 15.9 mm slit used to mask most of the incident neutron

336   beam. Neutrons were only allowed to pass through the slit, which was positioned

337   parallel to the line defining the visually observable rind-core interface. The 1 mm-

338   thick Cd mask was moved sequentially to scatter neutrons from areas of dimension 1

339   mm x 15.9 mm moving from the edge of the rind to the fresh rock (Fig. 6A, F).

340   However, because an orientation notch was cut into each section, the actual

341   illuminated sample area was reduced in the rind with respect to the fresh rock part in

342   which no notch was present. The varying illuminated areas were measured and

13

343   appropriate scaling factors applied ot normalize scattering intensities to the

344   respective sample volumes. The SANS data were corrected for neutron

345   transmission, empty quartz wafer scattering and blocked beam (dark current).

346   Normalization to the empty beam current was used for absolute scattering intensity

347   calibration (Kline, 2006).

348   Ultra-small angle neutron scattering (USANS) data were obtained on the BT5

349   beamline at NCNR NIST, Gaithersburg, USA for the same set of samples in a similar

350   fashion. The USANS data were corrected for empty cell scattering and transmission

351   and de-smeared using the NIST data reduction routines (Kline, 2006). Finally, the

352   corrected and normalized SANS and USANS data sets were combined into one

353   scattering curve as described in Jin et al. (2011).

354   In SANS and USANS, the scattered intensity, I(Q), is measured as a function

355   of the momentum transfer, defined as Q = (4π/λ) sin θ, with λ being the neutron

356   wavelength and 2θ the angle of scatter. Small angle scattering arises from

357   differences in neutron coherent scattering length density (SLD) between nm to μm

358   scale dispersed phases. Even for multimineralic rocks, it has been shown that the

359   dominant SANS/USANS scattering contribution results from the embedded pore

360   system and internal mineral-pore surfaces (two-phase approximation) (Anovitz et

361   al., 2009; Radlinski, 2006) . In this case, the porosity is obtained from the scattering

362   invariant, given by $Z = 2\pi^2\phi_1(1-\phi_1)(\rho_1^* - \rho_2^*)^2$,with ϕ_1 the porosity and ρ_1^* and ρ_2^* the

363   SLD's of pore and mineral phase, respectively. For empty connected and

364   unconnected pore spaces the SLD is zero. Application of fractal models has proven

365   very useful for the description of the multiscale porosity with rough internal surfaces

366   often found in rocks (Lo Celso et al., 2000; Triolo et al., 2000; Navarre-Sitchler and

14

367   Brantley, 2007). The determination of pore size distribution and internal surface area

368   is performed using the PRINSAS software, which is based on the polydisperse hard

369   sphere model (Hinde, 2004). SANS and USANS are uniquely suited to characterize

370   the nanoscale porosity and internal surface area of rocks in a statistically meaningful

371   way. Based on previous research (Anovitz et al., 2009; Jin et al., 2011), neutrons

372   scatter in porous rocks from both pores and bumps on the pore-mineral interface.

373   ,The linear dimension or spacing (Å) of these scatterers -- either pores or bumps --

374   equals 2.5/Q (Radlinski, 2006). Intensities of scattering at high Q ($1x10^{-3} < Q < 0.03$

375    $Å^{-1}$) measured by SANS, correspond to scatterers of diameter or spacing d, $1 < d <$

376   250 nm. USANS, measured at low Q ($3x10^{-5} < Q < 1x10^{-3}$ $Å^{-1}$), corresponds to

377   scatterer dimensions or spacings of 250 nm < d < 8.3 μm.

378   Both SANS and USANS data were measured on DR-4, but only SANS data

379   were collected successfully for DR-7. Due to high incoherent background at higher Q

380   for both samples, SANS spectra were considered only for the Q range of 0.002 –

381   0.05 A^{-1} (5 < d < 250 nm). For the total porosity calculation we used combined

382   SANS+USANS spectra for the Q range of $3x10^{-5} - 0.3$ $Å^{-1}$ (0.8 nm - 8.3 μm).

383

Results

Drilling Observations

386   Drilled boreholes revealed repeated zones of highly fractured rock embedded

387   within layers of disaggregated regolith material (Figure 4). In borehole B1W1, 2.1 m

388   of overburden (road-building material and regolith) overlay the first zone of rock.

389   From depths 2.1 m to 19 m, zones of rock and regolith alternate approximately every

15

390 2 m. Recovery of intact or fractured rock was only 8-60% for each 1.5 meter drilling

391 run that passed through rock, indicating that 40-92% of the volume contained void

392 space (fractures) or regolith (i.e., sample recovery percentages refer only to rock or

393 hard saprock recovery; regolith, which was recovered as mud, is not included here).

394 Recovery is given as 0% for zones shown as regolith in Figure 4, with the exception

395 of the zone at 14.5-16.0 m depth where a total of 0.3 m of saprock (weathered rock)

396 was recovered in several pieces. Between 19.0 and 33.5 m depth, neither rock nor

397 saprock were recovered. At 33.5 m depth, another zone of rock was sampled before

398 drilling was terminated at 37.2 m depth. Borehole B1W2 was drilled at slightly higher

399 elevation than B1W1 on the road but aligned with the spine of a ridge. This second

400 borehole passed through 4.1 m of disaggregated overburden (road fill or regolith)

401 before the first zone of rock was reached. From 4.1 to 13.4 m, rock recovery was

402 high (53-90% per 1.5 m drill run) and un-broken sections of core that were 0.3-, 0.46,

403 0.6-, and 0.9-m long were recovered in addition to numerous smaller pieces.

404 Throughout the drilling, recovery less than 100% indicated that some volume of

405 the drilled section was occupied by open fractures and/or regolith. In drilling runs

406 with low or zero recovery, wet mud was brought up by the coring apparatus – this

407 material was interpreted as regolith that had been liquefied by the water flushed into

408 the borehole to cool the drill bit.

409 Below 13.4 m depth in borehole B1W2 (Figure 4), recoverable rock was sparse,

410 with zero recovery between 16.5 and 25.3 m, i.e., regolith. However, small intact

411 saprock samples were recovered from between 13.1 and 14.8 m depth (11%

412 recovery) and between 15.7 and 16.3 m depth (30% recovery including 0.2 m of rock

413 fragments). At 25.3 m depth, another zone of rock was recovered before drilling was

414 terminated at 27.0 m depth.

16

415   Rock samples recovered from both the borehole drilling on the road and on the

416   exposed boulders are fine- to medium fine-grained, dark blueish or greenish grey

417   (Figure 2). The rocks recovered from the deep drilling contained abundant natural

418   fractures, many of which had weathering rinds that were up to 15 mm thick.

419   Weathering rinds appeared as thin, reddish coatings along the exposed fracture.

420

421   *Corestone measurements*

422   The exposed corestones measured here and cored using the hand-held drill,

423   were observed to have diameters of 0.5 – 3.0 m, although a few, partially buried

424   corestones were > 3.0 m (Table 1). Therefore, the corestone size, calculated as the

425   cube root of the measured volume, ranges from 0.5 – 2.6 m for the fully exposed

426   corestones. As shown in Figure 2, corestones exposed at the land surface had very

427   thin weathering rinds. These rinds were approximately 0.5 – 5.0 mm in thickness.

428   The corestones themselves were greyish-blue in color whereas the rinds appeared

429   whitish in thin section, terminating in reddish coloration toward the surface, similar to

430   the rinds along fracture surfaces in the deep borehole samples. Un-weathered

431   portions of the corestones were classified as fine-grained siltstone to coarse-grained

432   sandstone. Corestones appeared relatively devoid of fractures. Sampled corestone

433   size, elevation, and rind thicknesses are summarized in Table 1 with compositional

434   data for selected samples shown in Tables 2-4.

435

436   *Chemistry and mineralogy*

17

437   Most of the rock samples collected (exposed corestones and deep borehole

438   samples) can be chemically classified as basaltic-andesites based on the total alkali

439   vs. silica content (TAS), although a few fall into the range of basalts or andesites

440   (Table 2). Although visible grain size and color of un-weathered rocks vary slightly

441   within the Bisley watershed, the bulk chemical composition is not highly variable with

442   depth in the boreholes, between boreholes, or between boreholes and corestones

443   (Figure 5; Table 2). Relative to the borehole rock samples, regolith recovered from

444   the borehole cores had a higher CIA and contained less Ca, Na, Fe(II), and Mg and

445   slightly more total Fe and Ti (Table 2). Exposed corestones that were sampled with a

446   hammer appear more chemically variable than borehole samples, particularly in

447   labile elements such as Ca, Mg, Na, and K, which is reflected in the variability in the

448   CIA (Table 2, Figure 5A). Relative concentrations of elements that are commonly

449   retained during weathering (Fe, Al, Si) are similar in corestone and borehole samples

450   (Figure 5B).

451   Relative to the un-weathered rock, weathering rinds on the corestones are

452   typically depleted in Ca, Mg, Na, and Si and enriched by more than 50% in Fe and

453   hydrous components (LOI values) (Figure 6; Table 4). However, depletion of labile

454   elements begins inboard of the core-rind boundaries in some instances (Figure 6).

455   The CIAs of the rinds (~70) are higher than the CIAs of the cores (~60) and lower

456   than the CIAs of the saprock samples recovered from the boreholes (~80). The CIAs

457   of the hand-drilled cores (Table 4) are comparable to those of the subsurface

458   corestones (Table 2). This data is in agreement with microscopic observations of Fe-

459   rich material in the weathering rinds (Figures 7A-B).

460   Quantitative XRD analysis of visibly un-weathered rock samples from the B1W1

461   and B1W2 borehole cores revealed these rocks to be dominated by plagioclase and

18

462 chlorite with quartz, epidote, pyroxene, K-feldspar, tourmaline, and minor prehnite,

463 biotite, calcite, illite, and kaolinite (Table 3). The concentrations of quartz and epidote

464 vary to greater extent than other minerals although distinct variations with depth or

465 between boreholes is not observed (Figures 8 and 5C, Table 3).

466

Thin section observations

468   Analysis of thin sections from corestones and borehole core samples by SEM

469 revealed a complicated matrix that is spatially variable, with areas of microcrystalline

470 quartz or microcrystalline albite forming a groundmass that surrounds large pyroxene

471 crystals (Figures 9A-F). Less abundant microcrystalline K-feldspars are interspersed

472 in the groundmass. Chlorite largely occurs as wispy strands interspersed with

473 microcrystalline albite (Figure 9A). Accessory titanite (sphene), ilmenite, apatite, and

474 pyrite have also been identified (Figures 9A, C, E).

475   Optical microscope images of the corestone thin sections revealed highly

476 altered weathering rinds consisting of remnants of mineral grains (plagioclase and

477 pyroxene) in an opaque matrix, presumably Fe(III)-oxides or -hydroxides (Figures

478 7A, B). Fe-rich regions were also observed under SEM. Alteration is also apparent in

479 the visually non-weathered inner portions of the corestone samples, i.e., >10 mm

480 from the outer rind edge. In particular, extensive porosity development can be seen

481 in Fe(II)-rich minerals (amphibole, pyroxene, epidote) and to a lesser degree in

482 plagioclase. Amphiboles, present as inclusions within larger pyroxene crystals, are

483 extensively replaced with fine-grained chlorite (Figure 9B). SEM and optical images

484 of corestones also revealed preferential porosity development along plagioclase

19

485   grain boundaries and within epidote grains (Figure 10). Accumulation of opaque, Fe-

486   rich precipitate is observed within epidote pore space.

487

Neutron Scattering

489   Examples of neutron scattering data, taken on rind and core samples, are

490   given in Fig. 11A. In both samples (DR-4 and DR-7), the rinds had higher scattering

491   intensities than the cores. These higher intensities are indicative of higher porosity

492   and/or specific surface area (SSA) – both of which can be calculated from neutron

493   scattering data (Hinde, 2004) and both of which show an increase at the core-rind

494   interface. The same Q range (0.001 < Q < 0.05 Å^{-1}) was used for both samples to

495   determine nano-porosity (Table 5). The range in scatterer sizes that contribute to

496   SANS for this Q range is referred to here as nanoporosity (in contrast to "total

497   porosity" referred to below as inferred for SANS + USANS). For sample DR-4, SANS

498   and USANS for both weathered (rind) and un-weathered (core) areas, a break in

499   slope is observed on the log I – log Q plots at a scatterer dimension between 200

500   and 300 nm (Fig. 11A).

501   Some differences between samples were also observed. For example, DR-4

502   (from a corestone exhumed at a lower elevation) has higher porosity at large Q

503   (small scatterers) than DR-7 (from a higher elevation) at every position. In addition,

504   DR-7 exhibits smaller changes in porosity and SSA across the transects compared

505   to DR-4. It is furthermore striking that, relative to the interior core, the porosity and

506   SSA increases near the core-rind interface in DR-4 and then decreases in the outer

507   rind while steady increases only are observed for DR-7 (Fig. 6 B,G).

20

508   Total porosity was also calculated by combining SANS and USANS data

509   (scatterer dimensions in the range, 0.8 nm - 8.3 μm) for sample DR-4 (Table 5). Note

510   that these methods are only capable of measuring scatterers smaller than ~10 μm ,

511   so "total" does not include porosity or SSA attributed to larger scatterers (e.g., pores

512   > 10 μm). The total porosity of the protolith varies widely and is equal to 8.1 ± 4.1%

513   (an average of the 3 core measurements). Porosity increases by a factor of ~2.5x

514   across the core-rind interface but the decreases in the rind (Table 5). Therefore, the

515   data are consistent with larger scatterers (probed by USANS) forming deeper in the

516   core than smaller scatterers (probed by SANS). Interestingly, while SANS SSA did

517   not change much at the core-rind interface, the combined SANS+USANS SSA (total

518   SSA) exhibits a sharp increase at the interface. The SSA continues to grow and

519   becomes more than 3x larger than the protolith SSA towards the rind edge (Fig. 6G).

520

Discussion

Chemical Weathering

523   A history of low- to moderate-grade metamorphism is reflected in the Bisley

524   rocks by the presence of epidote, prehnite, pyrite, and tourmaline (Table 3, Figures

525   8-9). Additionally, microcrystalline quartz that is variable in abundance may reflect an

526   episode of metasomatism in which Si-rich fluids permeated the volcaniclastic

527   sediments non-uniformly (Figures 8 and 5C). Furthermore, all the Bisley rocks

528   contain abundant Mg-rich chlorite, which is commonly associated with low- to

529   medium-grade metamorphism and burial diagenesis. Therefore, replacement of

530   amphibole by chlorite in otherwise un-weathered zones is likely the result of

531   diagenetic or hydrothermal processes rather than weathering (Figure 9B).

21

532   In contrast to the metamorphism, weathering reactions are clearly observed in

533   the ~mm's thick weathering rinds that surround corestones and fractures. The highly

534   altered weathering rinds consist of remnants of grains of plagioclase and pyroxene in

535   an opaque matrix of Fe(III)-oxides or –hydroxides and secondary clay minerals

536   (Figures 7A, B). As expected, extensive porosity development can be seen in Fe(II)-

537   rich minerals (amphibole, pyroxene, epidote) and to a lesser degree in plagioclase.

538   However, inward from the core-rind boundaries, SEM and optical images also

539   revealed preferential porosity development along plagioclase and pyroxene grain

540   boundaries and within epidote, amphibole, pyroxene, and chlorite grains (Figures

541   7C, 9C, 10). Accumulation of opaque, Fe-rich precipitate is observed within epidote

542   pore space. Thus, weathering fronts of these five minerals (plagioclase, pyroxene,

543   epidote, amphibole, and chlorite) extend into the cores, inboard of the core-rind

544   boundary. The core-rind boundary may coincide with the transition from advective (in

545   the rind) to diffusive (in the core) transport of reactants (Ma et al., 2012; Sak et al.,

546   2004; Sak et al., 2010).

547   Plagioclase and chlorite make up about 25 and 36 wt% (Table 3),

548   respectively, of the visibly un-weathered corestones (exposed and subsurface) and

549   these minerals are largely absent from the saprolite and significantly weathered in

550   the weathering rinds. Hence the formation of disaggregated saprolite from rock is

551   primarily attributed to chemical weathering reactions involving these two minerals.

552   However, plagioclase or chlorite dissolution may not be the first chemical weathering

553   reaction in the rock. Pyrite was also observed in thin sections taken from un-

554   fractured sections of the deep drilled cores, but not in the sampled corestones or

555   weathering rinds. Two possible explanations are that 1) pyrite is heterogeneously

556   distributed in the bedrock or 2) pyrite weathering begins early and proceeds rapidly

22

557   such that no pyrite remains in the outer 20 cm of the corestones. The oxidation of

558   Fe(II) primary minerals has been indicated as the incipient weathering reaction in the

559   bedrock of other watersheds, including the quartz diorite of the neighboring Rio

560   Icacos watershed (Buss et al., 2008) and the shale of the Susquehanna Shale Hills

561   Critical Zone Observatory in central Pennsylvania (Brantley et al., Subm.). Thus

562   oxidation of Fe(II) in pyrite or one of the other Fe(II)-containing primary minerals may

563   be the initial weathering reaction. Alternatively, dissolution of minor calcite (Table 3)

564   may also control initial porosity development as has been shown to be the case for

565   granitoid rocks (White et al., 2005).

566

567   *Fracturing and Corestone Development*

568   Corestones exposed at the surface in the Bisley I watershed are generally

569   angular to sub-rounded. We nonetheless interpret them as corestones that formed in

570   the subsurface, starting as fracture-bounded bedrock blocks that were bathed in

571   infiltrating meteoric fluids. With chemical weathering and fracturing, the blocks are

572   inferred to have weathered in place, forming saprolite. However, we never observed

573   rinds thicker than about 5 mm at land surface. Therefore, as rinds form, they must

574   periodically slough or slake off. This mechanism is thus one way (or perhaps the

575   predominant way) that saprolite forms. The progression of bedrock to weathering

576   rind to saprolite is documented in the CIAs for the rock samples (~60), the corestone

577   rinds (~70) and the borehole saprock (~80). With that model, we can explain the

578   marked reduction of corestone size with elevation. In fact, no corestones are

579   observed above ~380 masl and no corestones are exposed at the ridgetop,

580   presumably because they have weathered away and only corestone-free saprolite

23

581   remains. Fletcher and Brantley (2010) modeled this process such that corestones

582   diminished in size as plagioclase chemically weathered at the corestone surface.

583   However, it is apparent from the data present here that both chemical and

584   mechanical weathering drives the disaggregation of the metavolcaniclastic rocks in

585   the Bisley watershed. This weathering may occur at the grain or grain aggregate

586   scale without rounding the corestones. Although occasional large exposed

587   corestones are observed to have split along nearly vertical fractures after exposure,

588   the angular forms of the corestones are not attributed to processes operative during

589   surface exposure but rather to their angular shape throughout their lifetimes below

590   and above ground. Indeed, oxidized weathering rinds were also observed along

591   relatively angular fractures throughout the drilled rock cores (Figure 12). Apparently,

592   corestone size diminution is occurring both by chemical weathering and

593   disaggregation of the rind surface, and splitting along fractures in otherwise intact

594   rocks. Almost all of this weathering and fracturing is occurring while the rock is in the

595   subsurface. Similar coupling between physical fracturing and chemical weathering

596   was observed in spheroidally weathering dolerites in South Africa, wherein Røyne et

597   al. (2008) found that chemical weathering reactions drive both corestone size

598   diminution and large-scale hierarchical fracturing by which corestones are broken

599   apart internally.

600   The nature of the physical weathering is further indicated here by the rinds on

601   corestone surfaces. No clear correlation between rind thickness and elevation is

602   apparent in the data collected from either exposed corestones or drilled cores (Table

603   1, Figure13). From Figure 13, it follows that rinds exposed to weathering may

604   normally detach when greater than about 6 mm in thickness. However, in landslide

605   scarps near the ridgetops, small (approx. 5-20 cm), angular corestone remnants that

24

606   had weathered all the way through were also observed to be buried within the

607   regolith. Thus it appears that with sufficient time in the subsurface, rind material

608   could completely consume a small (10-30 cm) corestone.

609   The quartz diorite bedrock of the neighboring Rio Icacos watershed weathers

610   spheroidally. The mechanism of this weathering has been attributed to reaction-

611   driven fracturing whereby O_2 diffuses into low porosity bedrock and oxidizes Fe(II)

612   within biotite, creating stress that leads to fracturing (Buss et al., 2008; Fletcher et

613   al., 2006). The volcaniclastic bedrock of the Bisley watershed has significantly less

614   biotite than the quartz diorite (0.9 and 9.5%, respectively, Table 3 and White et al.,

615   1998), which may explain the lack of spheroidal weathering in the Bisley watershed.

616   Instead, weathering rinds form and slough off via physical processes and weathering

617   does not become limited by diffusion through the rinds. The lack of rounding of the

618   corestones is consistent with sloughing off of the rind: other researchers have

619   noticed that diffusion-limited weathering of basaltic-andesitic clasts causes rounding

620   of the unaltered core (Ma et al., 2012). In contrast, in Bisley, the corestones remain

621   relatively angular perhaps because the weathering rinds fall off.

622

Porosity and Surface Area

624   Increasing porosity and SSA during weathering has been observed with

625   SANS and USANS for other weathering materials (Jin et al., 2011) and these

626   changes are well known from other porosity and surface area measurements (Schulz

627   and White, 1999; White and Brantley, 2003; White, 1990). The break in slope in plots

628   of log I - log Q (Fig. 11A) has also been observed in weathered and un-weathered

629   crystalline rocks (Bazilevskaya et al., this volume; Navarre-Sitchler et al., Subm.).

630   The break in slope has been attributed to different types of scatterers in rocks: at

25

631   high Q, scattering occurs at bumps on pore-grain interfaces and at low Q, scattering

632   occurs from pores that form within grains, on grain boundaries, and at triple grain

633   junctions. In other words, the distribution of sizes of interfacial nanometer-sized

634   bumps differs from the distribution of sizes of the larger pores. Given this

635   interpretation, one explanation is that the break in slope (here, 200-300 nm) roughly

636   corresponds to the smallest grain size or pore size in the rock. For example, no

637   break in slope has been observed in weathered and un-weathered shales where the

638   grain size is sub-micron (Jin et al., 2011).

639   Variations in porosity are attributed to the combined effects of dissolution and

640   precipitation in the rinds. For both samples subjected to neutron scattering analysis,

641   Ca and K depletion and Fe enrichment are documented by SEM-EDS (Fig. 6).

642   Interestingly, these reactions occur deeper within the core in DR-4 than DR-7, i.e.,

643   that sample (DR-4) started to weather in the visually non-weathered portion of the

644   corestone. Consistent with these data, porosity as measured with SANS and

645   SANS+USANS starts to increase with respect to the protolith at ~3.5 mm, well below

646   the visually observed core-rind interface in DR-4 (Fig. 6F-G). SEM images also

647   document mineral alteration deep in the corestone (Figures 9-10). These results

648   offer further evidence that weathering fronts do not necessarily coincide with

649   weathering rinds such that weathering processes (porosity development and mineral

650   alteration) may begin inboard of the visible rind.

651

652   *Critical Zone Geometry*

653   Two models for the geometry of the deep critical zone in the Bisley

654   watersheds have been proposed previously (Fletcher and Brantley, 2010;

26

655   Schellekens et al., 2004). Schellekens et al. (2004) utilized geo-electric sounding to

656   infer a subsurface structure that consists of 0.1-0.5 m of low-resistivity topsoil, 5-40

657   m of intermediate- to high-resistivity subsoil and saprolite; a deeper less-weathered,

658   low-resistivity saprolite 20-25 m thick, and finally bedrock below depths of 20-60 m.

659   Therefore, the depth of our boreholes, which terminated in rock at 27.0 and 37.2 m

660   below the ground surface, are consistent with the depth to bedrock predicted by

661   Schellekens et al. (2004). Although the resistivity data did not resolve the corestones

662   embedded within the saprolite, it captured a general picture of the subsurface that is

663   broadly consistent with our borehole data and the model of Fletcher and Brantley

664   (2010). It should be noted that the depth to bedrock could be even greater than the

665   depth of the boreholes as we cannot be certain that drilling terminated in bedrock

666   and not in corestones. However, the borehole profiles, the resistivity profiles, and the

667   models mentioned above all indicate that extensive weathering occurs at least 20 m

668   below the stream channel; thus weathering depth is not controlled by the local

669   stream level. In addition, highly oxidized saprolite and weathering rinds on the

670   fracture surfaces of deep subsurface corestones reflect the presence of water and

671   oxygen below the stream channel. Therefore, not all of the water in the watershed is

672   discharged to the Bisley I stream. Presumably groundwater is transported via deep

673   flowpaths and discharged to the larger tributary or Mameyes River at a lower

674   elevation.

675   Fletcher and Brantley (2010) proposed that prior to the onset of the recent

676   denudation regime, the ground surface and the bedrock weathering interface were

677   parallel to each other and that the stream channel incised the saprolite (exposing

678   corestones) until the relatively un-weathered bedrock was reached at low

679   elevationBorehole drilling confirmed the presence of subsurface corestones within

27

680　the depth-range predicted by the Fletcher and Brantley model.Presumably, the

681　corestones exposed at the surface are the remnants of the chemical weathering and

682　fracturing that began in the subsurface. Many of the subsurface corestones are

683　riddled with natural fractures, whereas exposed corestones tend to be massive.

684　Consistent with this, although we only measured and sampled the largest of the

685　aboveground corestones at any given locality (Table 1), many smaller corestones

686　were observed at all locations and these stones are candidates to have split off from

687　larger corestones along fracture surfaces.

688　　　　Differences in the degree of fracturing were observed between the two

689　boreholes. Zones of recoverable rock were larger and less fractured in borehole

690　B1W2, which was drilled in alignment with a ridge, compared to borehole B1W1,

691　which was drilled near the stream channel (Figure 4). In fact, roughly 30% of the

692　material drilled at B1W2 was rock, while only 13% of the drilled material from B1W1

693　was rock. This could indicate that subsurface corestones are larger under the ridge

694　than in the valley. Corestone size is a function of fracture spacing and duration and

695　extent of weathering. Subsurface corestones at the same elevation in the two

696　boreholes can reasonably be considered to have weathered for the same length of

697　time and thus the difference in corestone size may indicate wider fracture spacing

698　under the ridges – i.e., more resistant to weathering -- and narrower fracture spacing

699　under the valleys. If weathering and erosion are faster where fracture spacing is

700　closer and slower where fracture spacing is wider, as predicted by Fletcher and

701　Brantley (2010) and if the two boreholes are representative of the subsurface, then it

702　is furthermore possible that the valleys and ridges in the Bisley watersheds are

703　controlled by the fracture spacing of the underlying bedrock.

28

704   Of course, other interpretations are also possible. For example, if more water

705   flows through the subsurface under the valley than under the ridge, the additional

706   water flux could enhance the extent of weathering and weathering could drive

707   fracturing. Alternately, fracturing can be caused by geomporphic processes such that

708   channel incision and removal of material causes enhanced fracturing in the valley

709   bottom. Such differences in fracture distribution between valley floor and valley walls

710   have been observed elsewhere (Wyrick and Brochers, 1981). Alternatively, some

711   subsurface characteristics could be relict landslide material, particularly in local

712   topographic low areas, such as borehole site B1W1.

713   The distribution of subsurface corestones is also important for understanding

714   and predicting the distribution of nutrient pools. In our previous work on the

715   spheroidally weathering corestones of the nearby Rio Icacos watershed, we found

716   that the weathering flux of Fe(II) and P from primary minerals at the corestone-

717   regolith interface was sufficient to support a thriving subsurface microbial community

718   that was effectively isolated from the surface nutrient cycles by deep, highly leached

719   regolith (Buss et al., 2005; Buss et al., 2010). Similarly, soil organic matter (SOM)

720   content may be related to the location of subsurface corestones. Johnson et al.

721   (2011) measured SOM in soil pits (10-60 cm deep) dug at 84 locations throughout

722   the Bisley I watershed. Buried corestones limited effective soil depth to less than 60

723   cm in many of the pits, particularly in the valleys and on slopes. They found a

724   stronger correlation between the concentration of SOM from each depth sampled (0-

725   10 cm, 10-35 cm, 35-60 cm, and the combined 0-60 cm) and soil depth than to other

726   variables such as the C:N ratio of local leaf litter. They attributed the relationship

727   between SOM and soil depth to the greater stability (less erosion and disturbance) of

728   the land surface where the soils are deeper (i.e., on the ridge tops). This

29

729   phenomenon is not exclusive to the tropics. In the Green Mountains of Vermont,

730   USA, Johnson et al. (2009) also found a strong correlation between the

731   concentration of SOM at 20+ cm and soil depth (20 cm to the C-horizon, the depth of

732   which was not specified) and this was largely attributed to better draining of deeper

733   soils. Soil depth in the Green Mountains was also limited by boulders (from glacial

734   till) and the deeper soils were generally encountered at higher elevations,

735   comparable to what has been observed in the Bisley watershed.

736   **Conclusions**

737   We presented a case study where drilling allowed investigation of weathering

738   in the subsurface. We tested a model that was built upon the idea that weathering

739   had left a thick packet of weathered material that graded upward from relatively un-

740   fractured bedrock to corestones to saprolite to soil. Under this model, the Bisley I

741   channel is incising through this regolith package, exposing saprolite and corestones

742   at the land surface. Observations from this work that support the interpretation that

743   exposed corestones are relicts of earlier weathering include the following: i) Every

744   corestone analyzed had a weathering rind indicative of long-term exposure to

745   corrosive fluids. ii) Drilling through the inferred zone of weathering encountered

746   saprolite + corestones down to a depth of 37.2 m, equivalent to the inferred depth of

747   transition from saprolite+corestones to relatively un-fractured bedrock. iii) CIAs

748   document increasing degree of weathering such that subsurface and exposed

749   corestones are the least weathered, followed by rinds on corestones, then saprock

750   and finally, saprolite. Here, saprock refers to hand friable but intact weathered rock

751   recovered by borehole drilling. In addition, we present geochemical evidence and

752   neutron scattering data that are consistent with corestone diminution occurring via

753   dissolution of primary minerals coupled to physical weathering processes, i.e.,

30

754 formation of secondary porosity and detachment of weathering rinds >6 mm in

755 thickness. Finally, the angularity of each exposed corestone is consistent with

756 weathering rind formation followed by detachment. Detachment precludes diffusion

757 limitation during weathering which has been shown in other locations to cause

758 rounding.

759   The sequence of weathering processes for these volcaniclastic rocks is

760 inferred to be i) fracturing-induced exposure to meteoric fluids; ii) diffusion of

761 reactants from the fluid into the protolith at the fracture interface; iii) dissolution of

762 primary minerals (plagioclase, epidote, pyroxene, hornblende) and creation of

763 porosity at or below the core-rind interface iv) precipitation of Fe oxides that

764 decrease porosity in the outer part of the rind; and v) spalling of the altered surface

765 leaving relatively fresh protolith to again weather. Given this sequence, the fact that

766 DR-4 has higher nano-porosity (~5 < d <125 nm pores) as determined from SANS

767 data (Fig. 3) is attributed to the fact that it has recently spalled to create a new

768 surface rather than any differences in elevation or duration of weathering. The cycle

769 of weathering and spalling has been observed in basaltic material in other regions

770 (Hausrath et al., 2008). The lack of a porosity-elevation trend in the overall corestone

771 data is likely symptomatic of the fact that the timescale of the weathering-spalling

772 cycle is small compared to the overall duration of weathering of these corestones.

773 Therefore the thickness and chemical nature of each rind is indicative only of the

774 time since last spalling rather than the time since initiation of weathering of the entire

775 corestone. A detailed analysis of the mineral weathering reactions in these rocks will

776 be presented in a future paper.

777   Although geophysical techniques and surface observations provide a general

778 picture of the geometry and weathering processes of the watershed, deep drilling

31

779   revealed the following important details that could not have been known otherwise: i)

780   highly oxidized saprolite and fracture surfaces on corestones well below the

781   elevation of the stream channel indicate that the stream is not the outlet for all of the

782   water in the watershed; ii) the abundance of subsurface corestones and the degree

783   of fracturing of the subsurface corestones differs between the borehole drilled in the

784   valley and the borehole drilled under a ridge, suggesting that bedrock fracture

785   spacing could play a role in the development of topography; iii) intensively fractured

786   rock in the deep boreholes may indicate reaction-driven or other large-scale

787   fracturing as a primary saprolite formation mechanism that is not evident in surface

788   exposures. Therefore, although exposed corestones are interpreted here as relicts of

789   subsurface weathering, they do not provide a complete picture of the processes

790   occurring at depth. Finally, our results show that drilling is an invaluable tool for

791   characterizing the deep critical zone as it provides insights into the hydrology,

792   geomorphology, weathering, and nutrient cycles that impact the entire critical zone.

793

Acknowledgements

32

815

References

817   Anderson SP, Dietrich WE. 2001. Chemical weathering and runoff chemistry in a

818   steep headwater catchment. Hydrological Processes, **15**: 1791-1815.

819   Anderson SP, Dietrich WE, Brimhall GH. 2002. Weathering profiles, mass-balance

820   analysis, and rates of solute loss: Linkages between weathering and erosion

821   in a small, steep catchment. Geological Society of America Bulletin, **114**:

822   1143-1158.

823   Anovitz LM, Lynn GW, Cole DR, Rother G, Allard LF, Hamilton WA, Porcar L, Kim M.

824   2009. A new approach to quantification of metamorphism using ultra-small

825   and small angle neutron scattering. Geochimica et Cosmochimica Acta, **73**:

826   7303-7324.

827   Bazilevskaya E, Lebedeva M, Pavich M, Rother G, Parkinson D, Cole D, Brantley S.

828   this volume. Where fast weathering creates thin regolith and slow weathering

829   creates thick regolith. Earth Surface Processes and Landforms: In Press.

830   Brantley SL, Buss H, Lebedeva M, Fletcher RC, Ma L. 2011. Investigating the

831   complex interface where bedrock transforms to regolith. Applied

832   Geochemistry, **26**: S12-S15.

833   Brantley SL, Holleran ME, Jin L. Subm. Probing chemical reactions underlying the

834   Shale Hills Critical Zone Observatory, Pennsylvania (U.S.A.): Nested

835   weathering reaction fronts. Submitted to Earth Surface Processes and

836   Landforms.

837   Briggs RP, Cortes-Aguilar E. 1980. Geologic map of the Fajardo and Cayo Icacos

838   quadrangles, Puerto Rico. U.S. Geological Survey.

839   Brimhall GH, Dietrich WE. 1987. Constitutive mass balance relations between

840   chemical composition, volume, density, porosity, and strain in metasomatic

841   hydrochemical systems: Results on weathering and pedogenesis. Geochim et

842   Cosmochim. Acta, **51**: 567-587.

843   Bruijnzeel LA. 1991. Nutrient input-output budgets of tropical forest ecosystems: A

844   review. Journal of Tropical Ecology, **7**: 1-24.

845   Buss HL, Bruns MA, Schultz MJ, Moore J, Mathur CF, Brantley SL. 2005. The

846   coupling of biological iron cycling and mineral weathering during saprolite

847   formation, Luquillo Mountains, Puerto Rico. Geobiology, **3**: 247-260.

848   Buss HL, Mathur R, White AF, Brantley SL. 2010. Phosphorus and iron cycling in

849   deep saprolite, Luquillo Mountains, Puerto Rico. Chemical Geology, **269**: 52-

850   61.

34

851   Buss HL, Sak PB, Webb SM, Brantley SL. 2008. Weathering of the Rio Blanco

852   quartz diorite, Luquillo Mountains, Puerto Rico: Coupling oxidation,

853   dissolution, and fracturing. Geochim. Cosmoch. Acta, **72**: 4488-4507.

854   Calmels D, Galy A, Hovius N, Bickle M, West AJ, Chen M-C, Chapman H. 2011.

855   Contribution of deep groundwater to the weathering budget in a rapidly

856   eroding mountain belt, Taiwan. Earth and Planetary Science Letters, **303**: 48-

857   58.

858   Dietrich WE, Reiss R, Hsu M, Montgomery DR. 1995. A process-based model for

859   colluvial soil depth and shallow landsliding using digital elevation data.

860   Hydrological Processes, **9**: 383-400.

861   Dosseto A, Buss HL, Suresh PO. 2012. Rapid regolith formation over volcanic

862   bedrock and implications for landscape evolution. Earth and Planetary

863   Science Letters, **337-338**: 47-55.

864   Dosseto A, Turner SP, Chappell J. 2008. The evolution of weathering profiles

865   through time: New insights from uranium-series isotopes. Earth and Planetary

866   Science Letters, **274**: 359-371.

867   Eberl DD. 2003. User guide to RockJock - A program for determining quantitative

868   mineralogy from X-ray diffraction data. U.S. Geological Survey Open File

869   Report 03-78; 36 pp.

870   Eberl DD. 2008. User's guide to HandLens—A computer program that calculates the

871   chemistry of minerals in mixtures. USGS Open-File Report 2008-1244; 37 pp.

872   Fletcher RC, Brantley SL. 2010. Reduction of bedrock blocks as corestones in the

873   weathering profile: Observations and model. American Journal of Science,

874   **310**: 131-164.

35

875 Fletcher RC, Buss HL, Brantley SL. 2006. A spheroidal weathering model coupling

876   porewater chemistry to soil thicknesses during steady-state denudation. Earth

877   and Planetary Science Letters, **244**: 444-457.

878 Frizano J, Johnson AH, Vann DR. 2002. Soil phosphorus fractionation during forest

879   development on landslide scars in the Luquillo Mountains, Puerto Rico.

880   Biotropica, **34**: 17-26.

881 Garcia-Martino AR, Warner GS, Scatena FN, Civco DL. 1996. Rainfall, runoff and

882   elevation relationships in the Luquillo Mountains of Puerto Rico. Caribbean

883   Journal of Science, **32**: 413-424.

884 Hausrath EM, Treiman AH, Vicenzi E, Bish DL, Blake D, Sarrazin P, Hoehler T,

885   Midtkandal I, Steele A, Brantley SL. 2008. Short- and long-term olivine

886   weathering in Svalbard: Implications for Mars. Astrobiology, **8**: 1079-1092.

887 Heartsill-Scalley T, Scatena FN, Estrada C, McDowell WH, Lugo AE. 2007.

888   Disturbance and long-term patterns of rainfall and throughfall nutrient fluxes in

889   a subtropical wet forest in Puerto Rico. Journal of Hydrology, **333**: 472-485.

890 Heartsill-Scalley T, Scatena FN, Lugo AE, Moya S, Estrada Ruiz CR. 2010. Changes

891   in structure, composition, and nutrients during 15 yr of hurricane-induced

892   succession in a subtropical wet forest in Puerto Rico. Biotropica, **42**: 455-463.

893 Heimsath AM, Dietrich WE, Nishiizumi K, Finkel RC. 1997. The soil production

894   function and landscape equilibrium. Nature, **388**: 358-361.

895 Hinde AL. 2004. PRINSAS—a Windows-based computer program for the processing

896   and interpretation of small-angle scattering data tailored to the analysis of

897   sedimentary rocks. Journal of Applied Crystallography, **37**: 1020-1024.

36

898   Jin L, Rother G, Cole D, Mildner D, Duffy CJ, Brantley SL. 2011. Characterization of

899   deep weathering and nanoporosity development in shale - A neutron study.

900   American Mineralogist, **96**: 498-512.

901   Johnson KD, Scatena FN, Johnson AH, Pan Y. 2009. Controls on soil organic matter

902   content within a northern hardwood forest. Geoderma, **148**: 346-356.

903   Johnson KD, Scatena FN, Silver WL. 2011. Atypical soil carbon distribution across a

904   tropical steepland forest catena. CATENA, **87**: 391-397.

905   Jolly WT, Lidiak EG, Dickin AP, Wu T-W. 1998. Geochemical diversity of Mesozoic

906   island arc tectonic blocks in eastern Puerto Rico. Geol. Soc. Am. Spec. Pap.,

907   **322**.

908   Kline SR. 2006. Reduction and Analysis of SANS and USANS Data using Igor Pro.

909   Journal of Applied Crystallography, **39**: 895-9000.

910   Kurtz AC, Lugolobi F, Salvucci G. 2011. Germanium-silicon as a flowpath tracer:

911   Application to the Rio Icacos watershed. Water Resources Research: In

912   Press.

913   Lugolobi F, Kurtz AC, Derry LA. 2010. Germanium-silicon fractionation in a tropical,

914   granitic weathering environment. Geochimica et Cosmochimica Acta, **74**:

915   1294-1308.

916   Ma L, Chabaux F, Pelt E, Granet M, Sak PB, Gaillardet J, Lebedeva M, Brantley SL.

917   2012. The effect of curvature on weathering rind formation: Evidence from

918   Uranium-series isotopes in basaltic andesite weathering clasts in

919   Guadeloupe. Geochimica et Cosmochimica Acta, **80**: 92-107.

920   Navarre-Sitchler AK, Cole D, Rother G, Jin L, Buss HL, Brantley SL. Subm. Porosity

921   and surface area evolution during weathering of two igneous rocks.

922   Geochimica et Cosmochimica Acta.

37

923   Navarre-Sitchler A & Brantley S. 2007. Basalt weathering across scales. Earth and

924   Planetary Science Letters **261**: 321-334.

925   Nesbitt HW, Young GM. 1982. Early Proterozoic climates and plate motions inferred

926   from major element chemistry of lutites. Nature, **199**: 715-717.

927   Ollier C, Pain C. 1996. Regolith, Soils and Landforms. Wiley: UK; 326 pp.

928   Pike AS, Scatena FN, Wohl E. 2010. Lithological and fluvial controls on the

929   geomorphology of tropical montane stream channels in Puerto Rico. Earth

930   Surface Processes and Landforms, **35**: 1402-1417.

931   Radlinski AP. 2006. Small-angle neutron scattering and the microstructure of rocks.

932   In: Wenk HR (Editor), Neutron Scattering in the Earth Sciences. Reviews in

933   Mineralogy and Geochemistry. Mineralogical Society of America: Chantilly,

934   Virginia; pp. 363-397.

935   Riebe CS, Kirchner JW, Finkel RC. 2004. Erosional and climatic effects on long-term

936   chemical weathering rates in granitic landscapes spanning diverse climate

937   regimes. Earth and Planetary Science Letters, **224**: 547-562.

938   Roering JJ, Marshall J, Booth AM, Mort M, Jin Q. 2010. Evidence for biotic controls

939   on topography and soil production. Earth and Planetary Science Letters, **298**:

940   183-190.

941   Røyne A, Jamtveit B, Mathiesen J, Malthe-Sørenssen A. 2008. Controls on rock

942   weathering rates by reaction-induced hierarchical fracturing. Earth and

943   Planetary Science Letters, **275**: 364-369.

944   Sak PB, Fisher DM, Gardner TW, Murphy K, Brantley SL. 2004. Rates of weathering

945   rind formation on Costa Rican basalt. Geochimica Cosmochimica Acta, **68**:

946   1453-1472.

38

947   Sak PB, Navarre-Sitchler AK, Miller CE, Daniel CC, Gaillardet J, Buss HL, Lebedeva

948   MI, Brantley SL. 2010. Controls on rind thickness on basaltic andesite clasts

949   weathering in Guadeloupe. Chem. Geol.: In Press.

950   Scatena FN. 1989. An introduction to the physiography and history of the Bisley

951   Experimental Watersheds in the Luquillo Mountains of Puerto Rico. USDA

952   Forest Service: General Technical Report SO-72; pp. 22.

953   Scatena FN, Lugo AE. 1995. Geomorphology, disturbance, and the soil and

954   vegetation of two subtropical wet steepland watersheds of Puerto Rico.

955   Geomorphology, **13**: 199-213.

956   Schellekens JH, Scatena FN, Bruijnzeel LA, van Dijk AIJM, Groen MMA, van

957   Hogezand RJP. 2004. Stormflow generation in a small rainforest catchment in

958   the Luquillo Experimental Forest, Puerto Rico. Hydrol. Process., **18**: 505-530.

959   Schulz MS, White AF. 1999. Chemical weathering in a tropical watershed, Luquillo

960   Mountains, Puerto Rico; III. Quartz dissolution rates. Geochimica et

961   Cosmochimica Acta, **63**: 337-350.

962   Seiders VM. 1971. Geologic map of the El Yunque quadrangle, Puerto Rico. U.S.

963   Geological Survey.

964   Silver WL, Scatena FN, Johnson AH, Siccama TG, Sanchez MJ. 1994. Nutrient

965   availability in a montane wet tropical forest: Spatial patterns and

966   methodological considerations. Plant and Soil, **164**: 129-145.

967   Smith AL, Schellekens JH, Diaz AM. 1998. Batholiths as markers of tectonic change

968   in the northeastern Caribbean. Geol. Soc. Am. Spec. Pap., **322**: 99-122.

969   Tipper ET, Bickle MJ, Galy A, West AJ, Pomies C, Chapman HJ. 2006a. The short

970   term climatic sensitivity of carbonate and silicate weathering fluxes: Insight

971   from seasonal variations in river chemistry. Geochimica et Cosmochimica

972   Acta, **70**: 2737-2754.

973 Tipper ET, Galy A, Bickle MJ. 2006b. Riverine evidence for a fractionated reservoir

974   of Ca and Mg on the continents: Implications for the oceanic Ca cycle. Earth

975   and Planetary Science Letters, **247**: 267-279.

976 Triolo F, Triolo A, Agamalian M, Lin J-S, Heenan R, Lucido G, Triolo R. 2000, Fractal

977   approach in petrology: combining ultra small angle, small angleand

978   intermediate angle neutron scattering: Journal of Applied Crystallography, **33**:

979   863-866.

980 USDA NCRS. 2002. Soil Survey of Caribbean National Forest and Luquillo

981   Experimental Forest, Commonwealth of Puerto Rico. USDA, Natural

982   Resources Conservation Service: Washington D.C.; pp. 181.

983 West AJ, Galy A, Bickle M. 2005. Tectonic and climatic controls on silicate

984   weathering. Earth and Planetary Science Letters, **235**: 211-228.

985 White AF. 2002. Determining mineral weathering rates based on solid and soute

986   weathering gradients and velocities: application to biotite weathering in

987   saprolites. Chemical Geology, **190**: 69-89.

988 White AF, Blum AE, Schulz MS, Vivit DV, Stonestrom DA, Larsen M, Murphy SF,

989   Eberl D. 1998. Chemical weathering in a tropical watershed, Luquillo

990   Mountains, Puerto Rico: I. Long-term versus short-term weathering fluxes.

991   Geochimica et Cosmochimica Acta, **62**: 209-226.

992 White AF, Brantley SL. 2003. The effect of time on the experimental and natural

993   weathering rates of silicate minerals. Chemical Geology, **202**: 479-506.

40

994   White AF, Peterson, M. L. 1990. Role of reactive surface area characterization in geochemical models. In: Melchior DL and Bassett RL (Editors), Chemical modeling of aqueous systems II. Am Chem Soc Symp Ser; pp. 461-475.

997   White AF, Schulz MS, Lowenstern JB, Vivit D, Bullen TD. 2005. The ubiquitous nature of accessory calcite in granitoid rocks: Implications for weathering and solute evolution, and petrogenesis. Geochimica et Cosmochimica Acta, **69**: 1455-1471.

1001   Wyrick GG, Brochers JW. 1981. Hydrologic effects of stress-relief fracturing in an Appalachian valley. U.S. Geological Survey Water Supply Paper, **2177**: 51 pp.

1003   Ziegler K, Chadwick OA, White A, Brzezinski MA. 2005. $\delta^{30}Si$ systematics in a granitic saprolite, Puerto Rico. Geology, **33**: 817-820.

1005

41

Table 1. Physical Characteristics of Exposed Corestones

Sample	Elevation, (m)	Position	Dimensions (m)	Max. Size[1], (m)	Rind thickness, (mm ± stdev)	Notes
DR13	234	Stream channel	2.5 x 2 x 2	2.2	0	Fine-grained meta- siltstone; greenish color; pockmarked
DR12	235	Stream channel	2 x 2.5 x 2	2.2	0	Coarse-grained meta-sandstone; greenish color
DR11	247	Stream channel	3 x 0.5 x 1	1.1	1.1±0.1	Fine-grained meta- siltstone
DR10	248	Ridgetop	2 x 1 x 0.75	1.1	2.8±0.7	Coarse-grained meta- sandstone
DR2	263	Slope	> 3	>3	0	Coarse-grained meta- sandstone; dark color
DR1	281	Stream channel	> 3	> 3	0	Fine-grained meta- siltstone
DR3	312	Stream channel	3 x 3 x 2	2.6	1.6±0.3	Coarse-grained meta- sandstone
DR4	314	Edge of stream channel	1.5 x 1.5 x 1.5	1.5	3.3±0.3	Fine-grained meta- siltstone
DR5	319	Stream channel	1 x 0.5 x 0.5	0.6	9.2±2.2	Coarse-grained meta- sandstone
DR6	328	Stream channel	1.5 x 0.5 x 0.5	1.6	4.0±0.4	Fine-grained meta- siltstone
DR7	350	Slope	1.5 x 2 x 1.5	1.7	4.3±0.8	Fine-grained meta-siltstone
DR9	352	Slope	1 x 0.5 x 0.5	0.6	2.1±0.2	Fine-grained meta-siltstone
DR8	369	Stream channel	0.5 x 0.5 x 0.5	0.5	2.1±0.5	Coarse-grained meta-sandstone

[1] Corestone size calculated as the cubic root of corestone volume.

1006

1007

1008

42

Table 2. Bulk Chemistry of Exposed and Subsurface Corestones

Depth (m)	Al_2O_3 (wt %)	CaO	Fe_2O_3 total Fe	FeO[1]	K_2O	MgO	MnO	Na_2O	P_2O_5	SiO_2	TiO_2	Ba (ppm)	Nb	Sr	Zn	Zr	CIA[2]
Exposed Corestones[3]																	
-	16.1	6.24	8.40	4.40	0.66	4.76	0.15	3.96	0.17	54.20	0.62	430	40	230	90	117	59.7
-	16.6	7.20	7.73	4.30	0.69	4.73	0.14	4.50	0.18	55.60	0.62	420	30	280	90	86	57.3
-	16.7	5.10	9.58	5.50	0.77	5.92	0.17	5.00	0.2	53.00	0.63	580	20	290	100	86	60.6
-	17.8	3.90	7.67	2.90	2.78	3.69	0.16	1.47	0.12	50.30	0.57	520	10	220	140	463	68.6
-	17.6	2.01	12.1	-	0.42	5.16	0.2	4.2	0.12	48.8	0.81	230	<10	150	129	100	72.6
-	17.8	5.37	8.88	-	0.78	4.8	0.2	4.7	0.08	50.7	0.66	720	10	280	60	70	62.1
-	18.8	6.15	8.70	-	0.60	4.45	0.2	2.9	0.12	48.9	0.65	940	10	310	97	70	66.1
-	17.5	7.08	8.84	-	0.51	4.84	0.2	4.1	0.14	50.5	0.65	270	<10	200	58	70	60.0
-	17.5	7.18	9.73	-	0.38	5.79	0.1	4.5	0.18	48.8	0.73	60	<10	150	110	120	59.2
-	17.8	13.9	6.49	-	1.28	1.98	0.1	2	0.14	52.7	0.5	110	<10	120	16	90	50.9
-	18.0	9.36	9.39	-	0.71	4.79	0.2	4.1	0.14	52	0.68	220	10	250	58	120	56.0
-	18.2	11.6	8.60	-	0.13	3.96	0.1	4.3	0.19	53.6	0.7	40	10	150	50	120	53.2
-	14.7	6.69	7.90	-	1.18	4	0.1	2.4	0.14	57.8	0.69	520	<10	450	62	110	58.9
-	15.6	4.18	8.49	-	1.25	3.68	0.1	2.3	0.24	55.4	0.75	560	<10	370	70	130	66.9
-	25.9	0.04	8.18	-	0.09	0.32	0.0	0	0.15	45.5	0.74	100	<10	<10	24	120	99.5
-	20.6	0.02	12.0	-	0.15	0.25	0.0	0	0.17	47.9	1.08	120	<10	<10	<5	180	99.2
Subsurface Corestones B1W1, Elevation 261 masl[4]																	
2.1	17.5	7.77	8.94	5.9	0.62	6.22	0.12	2.2	0.11	53.6	0.68	330	<10	640	79	90	62.3
3.4	15.9	8.19	7.83	6.2	0.53	4.31	0.55	4.3	0.14	53.4	0.65	340	<10	280	79	110	55.0
4.00	18.1	9.26	8.14	6.20	0.35	4.14	0.14	3.60	0.11	53.3	0.58	290	<10	290	76	70	57.8
11.0	16.2	5.62	7.90	6.00	1.88	4.13	0.09	1.50	0.14	59.3	0.60	820	<10	540	89	90	64.3
12.8	18.1	1.89	10.8	<0.1	1.61	3.55	0.16	0.40	0.10	47.5	0.96	1070	<10	160	135	130	82.3
15.5	20.3	1.16	9.92	<0.1	1.22	2.92	0.15	0.70	0.07	49.7	0.64	1000	<10	130	96	70	86.8
16.5	13.9	5.75	7.4	5.70	1.09	5.17	0.10	2.20	0.10	60.6	0.59	570	<10	440	65	80	60.6
16.7	16.9	7.20	9.9	7.50	1.30	7.59	0.14	2.70	0.11	50.9	0.73	570	<10	530	112	100	60.1

43

17.0	17.5	8.78	8.90	6.80	0.29	5.87	0.13	3.90	0.10	50.0	0.65	300	<10	350	80	60	57.4
17.4	16.9	9.16	8.62	7.00	0.18	5.58	0.13	4.10	0.08	49.8	0.61	80	<10	360	78	50	55.7
18.0	17.2	10.80	9.0	4.40	0.81	5.28	0.13	3.00	0.10	51.0	0.65	250	<10	410	76	50	54.1
36.0	17.9	7.24	9.16	7.40	1.51	5.88	0.14	2.20	0.11	50.4	0.73	800	<10	570	84	100	62.0
37.0	17.6	7.53	9.20	7.00	1.44	6.38	0.14	2.20	0.10	53.0	0.70	700	<10	590	79	80	61.2

Subsurface Corestones B1W2, Elevation 263 masl

4.4	16.7	7.58	9.13	6.30	0.62	5.79	0.12	2.10	0.11	52.1	0.66	290	<10	630	69	90	61.9
6.4	17.0	8.69	7.86	4.90	0.41	5.03	0.10	2.40	0.11	52.8	0.64	190	<10	630	68	90	59.6
8.4	16.9	7.38	7.85	5.90	0.53	4.52	0.10	2.60	0.10	52.9	0.62	240	<10	580	62	90	61.7
10.4	17.9	7.90	8.05	5.30	0.54	4.88	0.10	2.10	0.11	56.1	0.69	360	<10	900	68	100	62.9
12.0	16.8	6.80	8.15	6.10	0.58	5.22	0.11	2.30	0.10	54.0	0.62	360	<10	780	65	90	63.4
14.0	18.9	4.20	10.90	0.40	0.87	3.45	0.10	1.60	0.13	50.0	0.78	840	<10	500	86	90	73.9
15.8	16.5	8.00	9.8	5.90	0.89	6.64	0.14	3.10	0.20	51.7	0.67	510	<10	690	74	70	57.9
26.7	15.8	8.62	9.2	5.40	0.77	6.01	0.14	3.10	0.11	50.6	0.63	360	<10	540	74	70	55.9

[1]Ferrous Fe not determined for all samples.

[2]CIA = chemical index of alteration = $100(Al_2O_3)/(Al_2O_3+CaO+Na_2O+K_2O)$ (Nesbitt and Young, 1982).

[3]Exposed corestones in this table were sampled with a hammer (not a drill).

[4]Subsurface corestones in this table are rock samples, exclusive of weathered fractures, returned via wire-line during borehole drilling. Shaded rows indicate saprock samples recovered during drilling.

44

Table 3. Mineralogy of Exposed and Subsurface Corestones

Depth (m)	Quartz (wt. %)	K-spar	Plag	Oxides	Kaol	Chlorite	Amph	Pyx	Tourm	Calcite[1]	Epidote	Prehnite	Biotite/ Illite[2]
Exposed Corestones[3]													
-	6.9	6.2	46.6	0.0	0.0	24.5	2.2	10.5	-	-	-	-	3.2
-	25.4	7.9	22.3	0.5	6.6	21.3	1.9	3.0	2.9	-	1.0	4.2	1.9
-	21.6	5.6	31.3	0.3	0.3	23.0	0.4	6.1	2.4	-	0.5	5.3	1.2
-	1.0	3.2	38.6	0.0	0.8	16.3	1.9	11.5	0.9	-	20.2	0.5	2.1
-	11.2	9.5	10.8	0.0	0.8	2.0	1.8	11.6	3.8	-	35.1	4.5	2.6
-	0.9	1.5	42.2	0.0	1.4	26.2	1.2	9.9	0.0	-	11.9	0.0	1.5
-	5.9	2.5	41.0	0.1	1.3	26.4	0.3	6.9	0.9	-	0.1	10.6	2.0
-	9.5	2.4	30.4	0.0	5.2	20.3	0.6	5.4	2.6	-	1.6	15.5	4.5
-	4.3	3.5	43.9	0.1	1.7	30.3	1.7	8.0	0.0	-	2.4	0.7	1.2
-	5.3	1.9	39.5	0.0	2.4	28.8	0.0	3.8	0.0	-	0.4	16.3	0.3
Drilled Bedrock B1W1, Elevation 261 masl													
2.1	17.5	4.0	33.2	-	0.9	24.5	-	7.3	1.0	0.1	11.4	0.0	0.2
3.4	6.6	4.7	43.4	-	0.2	18.6	-	11.5	3.0	4.7	3.0	4.3	0.0
4.00	7.3	3.4	35.4	-	0.0	21.8	-	6.4	2.9	0.9	4.4	16.5	0.9
11.0	13.2	15.4	35.2	-	0.0	25.0	-	3.4	3.1	0.0	4.0	0.0	0.5
16.5	6.1	9.6	37.3	-	1.0	26.1	-	12.7	4.4	0.3	1.8	0.7	0.0
16.7	4.0	9.0	34.0	-	0.6	28.7	-	14.6	5.9	0.2	1.4	1.0	0.7
17.0	0.0	5.4	42.4	-	0.1	35.4	-	11.9	2.8	0.3	1.7	0.0	0.0
17.4	1.1	2.6	46.2	-	0.0	23.2	-	11.7	2.5	2.6	2.0	8.0	0.0
18.0	4.8	6.2	31.4	-	0.8	16.1	-	14.9	2.4	0.3	22.2	0.0	0.9
36.0	7.1	10.7	39.5	-	0.4	30.9	-	6.5	2.3	0.4	1.6	0.5	0.0
37.0	13.2	10.8	30.1	-	0.8	27.2	-	10.5	5.1	1.1	0.7	0.1	0.2
Drilled Bedrock B1W2, Elevation 263 masl													
4.4	15.2	3.8	31.4	-	0.3	25.0	-	7.5	5.4	0.2	10.6	0.0	0.6
6.4	14.6	2.5	30.1	-	0.1	20.4	-	8.5	3.7	0.6	18.5	0.0	0.9

8.4	15.9	1.3	41.3	-	0.0	19.9	-	5.8	3.0	1.3	9.6	1.2	0.9
10.4	19.4	2.7	32.9	-	0.0	22.2	-	4.6	4.7	0.1	11.8	0.2	1.4
12.0	18.2	3.3	34.1	-	0.7	22.9	-	4.4	4.1	0.1	10.7	0.0	1.4
15.8	6.8	4.5	36.0	-	0.8	18.9	-	13.3	3.3	0.3	10.6	0.0	5.6
26.7	5.9	3.6	35.9	-	1.2	18.9	-	14.2	4.7	0.3	13.1	0.0	2.1

1016   [1]Dashed lines indicate that the mineral was not detected in the sample set.

1017   [2]Biotite and illite were not definitively identified separately.

1018   [3]Exposed corestones in this table were sampled with a hammer (not a drill).

1019

46

Table 4. Chemical Changes Across Core-Rind Interfaces

Sample[1]	Elevation (m)	Al_2O_3 (wt %)	BaO	CaO	Fe_2O_3 Total Fe	K_2O	MgO	MnO	Na_2O	P_2O_5	SiO_2	SrO	TiO_2	LOI (900C)	Zr (ppm)	CIA[3]
dr-10 core	248	19.2	0.06	5.36	8.69	1.25	4.61	0.16	4.62	0.13	52.3	0.05	0.74	2.90	80	61.3
dr-10 rind		18.8	0.08	2.09	15.85	1.44	4.17	0.27	3.26	0.12	43.1	0.03	0.92	11.68	104	73.5
% difference[2]		-2.3	35.3	-61.0	82.4	15.3	-9.5	68.9	-29.3	-5.9	-17.6	-43.0	23.2	302.9	30.3	
dr-7 core	350	17.3	0.09	7.18	9.31	0.89	5.07	0.16	4.15	0.11	52.1	0.04	0.68	2.84	85	58.6
dr-7 rind		17.3	0.12	5.30	10.46	1.04	5.09	0.25	3.95	0.12	50.5	0.03	0.77	6.76	91	62.7
% difference		-0.1	38.0	-26.1	12.3	17.1	0.4	54.5	-4.7	3.6	-3.1	-16.1	12.2	138.0	7.3	
dr-8 core	369	17.7	0.26	7.61	8.95	1.08	5.24	0.15	4.05	0.10	50.4	0.03	0.64	2.78	70	58.1
dr-8 rind		19.5	0.31	2.89	13.76	1.21	3.76	0.13	2.77	0.12	42.2	0.02	0.77	11.71	85	73.9
% difference		10.7	18.7	-62.0	53.8	11.2	-28.2	-9.1	-31.7	12.3	-16.4	-30.5	21.2	320.7	21.1	

1020   [1]Samples taken from corestones in Bisley stream channel using a hand-held paleomagnetic drill.

1021   [2]Percent differences in concentration between cores and the corresponding weathering rinds were calculated as $(C_{rind}-C_{bulk})100/C_{bulk}$. Negative values indicate

1022   depletion in the rind relative to the core, while positive values indicate enrichment.

1023   [3]CIA = chemical index of alteration = $100(Al_2O_3)/(Al_2O_3+CaO+Na_2O+K_2O)$ (Nesbitt and Young, 1982).

1024

47

1025   **Table 5. Neutron Scattering Data**

Distance[a] (mm)	Region	Density[b] (g cm^{-3})	SLD[c] (Å)	Porosity[d] (%)	Total[e] Porosity (%)	SSA[f] (m^2 g^{-1})	Total SSA (m^2 g^{-1})
Sample DR-7							
0.5	rind	3.10	4.05	1.16	na	0.89 ± 0.09	na
1.5	rind	3.10	4.05	1.14	na	0.65 ± 0.07	na
2.5	rind	3.10	4.05	1.09	na	0.63 ± 0.06	na
3.5	core	3.08	3.99	0.73	na	0.50 ± 0.05	na
4.5	core	3.08	3.99	0.78	na	0.55 ± 0.06	na
9.5	core	3.08	3.99	0.75	na	0.48 ± 0.05	na
Sample DR-4							
0.5	rind	3.16	4.14	2.65	13.8 ± 11.2	0.70 ± 0.07	4.57
1.5	rind	3.16	4.14	4.07	7.1 ± 2.0	0.91 ± 0.09	2.84
2.5	rind	3.16	4.14	5.12	22.4 ± 11.8	0.81 ± 0.07	1.65
3.5	core	3.08	4.14	2.48	7.6 ± 3.0	0.51 ± 0.06	1.36
4.5	core	3.08	4.01	1.67	12.4 ± 5.3	0.53 ± 0.05	1.44
9.5	core	3.08	4.01	1.86	4.2 ± 1.6	0.56 ± 0.06	na

1026   [a] Average distance from the edge of the outer edge of the weathering rind.

1027   [b] Mineral density determined from bulk chemical composition reported in Table 4.

1028   [c] SLD = Scattering length difference

1029   [d] Porosity determined from SANS = Small Angle Neutron Scattering (0.002 < Q < 0.05 Å^{-1}). [e]

1030   Total porosity of DR-4 was determined from the combined SANS + USANS (Q range: 1x10^{-3} <

1031   Q < 0.3 Å^{-1}). Error bars on total porosity indicate 95% confidence interval.

1032   [f] SSA = Specific surface area determined from SANS. Total SSA = SSA determined from the

1033   combined SANS + USANS data.

1034

1035

1036

Figure Captions

Figure 1. Map of volcaniclastic Bisley watersheds I and II. Quebradas I, II, and III are the Bisley streams. The two drilled boreholes are B1W1 and B1W2. *(Figure supplied in color for online publication).*

Figure 2. A. Simplified schematic view of a 100 m-thick weathering profile of *in situ* weathered bedrock blocks (corestones) underlying boulder-free saprolite, with the bedrock-corestone interface shown as horizontal. The first stage of critical zone development in the Bisley watershed is shown on the left, where corestones are shown schematically to decrease in size toward the land surface due to increased duration of weathering. The second stage of critical zone development is shown on the right, where corestones are exposed by a later episode of rapid erosion. **B.** Thick sections from corestones from different elevations in Bisley profile, Puerto-Rico. The outermost edge (top of the slides) shows the weathering rind development in cross-section. *(Figure supplied in color for online publication).*

Figure 3. A plot of the profile of the Bisley I stream channel (after Fletcher and Brantley, 2010). Below ~220 masl, the Bisley I joins with the Bisley II and III tributaries. The combined stream joins the Rio Mameyes along a bedrock-lined channel just above 50 masl. Fletcher and Brantley (2010) observed that the maximum size of corestones did not vary below 200 masl, but decreased with increasing elevation above 200 masl. Below 200 masl, the slope of the Bisley channel is invariant until joining with the river at 50 masl. The plane of the channel between 50 and 200 masl was interpreted to be the plane across which corestones emerge from the fractured bedrock, or the saprolite-bedrock interface. If the

49

1
2
3
4
5
6
7
8
9
10
11
12
13
14
15
16
17
18
19
20
21
22
23
24
25
26
27
28
29
30
31
32
33
34
35
36
37
38
39
40
41
42
43
44
45
46
47
48
49
50
51
52
53
54
55
56
57
58
59
60

1060   weathering profile is roughly parallel to the bedrock-saprolite interface (as shown),

1061   the average weathering profile thickness is 135 m.

1062   **Figure 4.** Diagram of boreholes drilled in the Bisley 1 watershed showing locations

1063   of recovered rock samples. Grey = fractured rock; white = granular material (i.e.,

1064   saprolite or sediment). Regolith zones were mostly washed out during drilling without

1065   sampling although a few intact pieces of saprock were recovered. All rock recovered

1066   was highly fractured with fractures spaced at mms to cms. Dashed lines at bottom of

1067   the cores indicate the deepest extent of drilling into what is inferred here to be

1068   relatively un-weathered bedrock.

1069   **Figure 5.** Ternary diagrams of Bisley rocks sampled from deep drilled boreholes or

1070   aboveground corestones. Data plotted here is for visibly un-weathered subsamples

1071   (weathered rinds were cut off before analysis). **A)** Borehole samples contain similar

1072   amounts of labile elements Ca, Mg, Na, and K, whereas corestone samples contain

1073   variable amounts of these elements indicative of weathering of some samples. **B)**

1074   Relative solid-state concentrations of total Fe, Al, and Si are similar in both borehole

1075   and corestone samples. **C)** High relative concentrations of quartz may be indicative

1076   of weathering in some of the corestone samples or evidence of hydrothermal

1077   alteration. *(Figure supplied in color for online publication).*

1078   **Figure 6. A-E)** Data from corestone DR-7 (350 masl). **F-J)** Data from corestone DR-

1079   4. Vertical axis on all panels A-J is the distance from the outer edge of the weathered

1080   rind, in mm. **(A, F)** Photographs of thick sections with lines marking 1 mm spacing.

1081   **(B, G)** Changes in porosity and specific surface area (SSA) determined from neutron

1082   scattering data and normalized relative to the protolith (i.e., 9.5 mm). SSA (open

1083   triangles) determined from SANS data. Total SSA (closed triangles), measured only

50

1084   on DR-4 (314 masl), was determined from SANS+USANS data. Note that these

1085   methods are only capable of measuring scatterers smaller than ~10 μm , so "total"

1086   does not include porosity or SSA attributed to larger scatterers (e.g., pores > 10 μm).

1087   **(C-E, H-J)** Tau values for major elements were calculated from EDS data using Al as

1088   an immobile element. Parent composition was chosen as an average of the

1089   compositions measured at ~6-8 mm from the rind edge, which were assumed to

1090   represent un-weathered rock based on visual observation *(Figure supplied in color*

1091   *for online publication).*

1092   **Figure 7.** Optical microscope images (20X magnification) of corestone sample DR-3,

1093   which consists mostly of anhedral large grains of plagioclase, smaller pyroxene

1094   grains, and occasional biotite grains. **A)** Weathering rind – bulk rock interface, **B)**

1095   The weathering rind contains fine-grained opaque minerals; large, a highly

1096   weathered pyroxene grain and small, white irregular grains, which may be

1097   disintegrating plagioclase. **C)** The bulk rock (10 mm inward from the weathering rind)

1098   contains patches of a brown-greenish stain within plagioclase and pyroxene grains

1099   and inter-grain cracks. **D)** Biotite grain and chlorite-stained plagioclase in the bulk

1100   rock (15 mm from the edge). Abbreviations: Pl – plagioclase; Px – pyroxene, Bi –

1101   biotite. *(Figure supplied in color for online publication).*

1102   **Figure 8.** Box and whisker diagram showing mineral contents of 18 visibly un-

1103   weathered core samples from boreholes B1W1 and B1W2 as determined by

1104   quantitative XRD (Eberl, 2003). Wide boxes indicate 25-75% of data and are divided

1105   by a line denoting 50%. Small boxes indicate the mean, whiskers extend to outliers,

1106   X symbols indicate 1-99% of the data and small horizontal lines indicate maximum

1107   and minimum values. Mineral names are abbreviated as follows: Plag = plagioclase,

51

1108   Chl = chlorite, Qtz = quartz, Pyx = pyroxene, Epi = epidote, Kspar = K-feldspar, Tour

1109   = tourmaline, Prehn = prehnite, Biot = biotite, Cal = calcite, Kaol = kaolinite.

1110   **Figure 9.** Backscattered SEM images of visibly un-weathered zones within a

1111   corestone rock sample from the Bisley 1 stream (A-C), a corestone exposed by a

1112   landslide (D), and core recovered from borehole B1W2 at ~8.4 m depth (E-F). **A)**

1113   Microcrystalline quartz (Qtz) and microcrystalline albite (Alb) are separated by a

1114   band of Fe, Mg chlorite (Chl). A biotite (Biot) crystal contains small inclusions of

1115   apatite. **B)** Amphibole (Amph) is visible embedded within clinopyroxene (Pyx),

1116   identified as augite. The interior of the amphibole crystals is altered to chlorite. **C)**

1117   Large pyroxene crystals are shown containing inclusions of titanite (sphene, Sph)

1118   and ilmenite (Ilm). **D)** Epidote (Epi) is distributed within microcrystalline quartz (Qtz).

1119   K-feldspar (KSpar) is also visible. **E)** Several zones of pyrite (Pyr) were found in this

1120   section of core. **F)** Crystals of calcic plagioclase (Plag) and pyroxene are shown

1121   surrounded by a groundmass of plagioclase, chlorite, titanite, and possibly other

1122   minerals. Images A-D were collected at the USGS in Menlo Park, CA. Images E-F

1123   were collected at the University of Bristol.

1124   **Figure 10.** Secondary Electron SEM image of corestone sample DR-7 taken 23 mm

1125   from the rind edge showing preferential porosity development within an epidote

1126   grain.

1127   **Figure 11. A)** Neutron scattering data, I versus Q, for the rind (2.5 mm from the

1128   outer edge of the rind) and core (9.5 mm from the outer edge of the rind) of

1129   corestone sample DR-4. The rind has a higher scattering intensity due to higher

1130   porosity. Q regions for SANS and USANS and corresponding scatterer diameter

1131   (pore size) are also shown. **B)** SANS spectra for corestone sample DR-7, with

52

1132   distances in mm from the outer edge of the rind. The data from 9.5 mm represents

1133   the fresh rock. *(Figure supplied in color for online publication)*

1134   **Figure 12. A)** Photograph of a section of rock core from borehole B1W2 ~5.5 m

1135   below the ground surface. A weathering rind is visible along a natural fracture. **B)**

1136   Close up image of the rind shown in A. *(Figure supplied in color for online*

1137   *publication).*

1138   **Figure 13.** Rind thickness (mm) versus elevation (masl) for rock samples collected

1139   from exposed corestones and boreholes. Trends in rind thickness as a function of

1140   elevation are not apparent in either set of data, likely due to spalling off of thick rinds

1141   on exposed corestones at higher elevation. The R^2 is 0.12 for the borehole data,

1142   0.42 for the corestone data (omitting the outlier), and 0.18 for the entire dataset

1143   (omitting the outliers).

1
2
3
4
5
6
7
8
9
10
11
12
13
14
15
16
17
18
19
20
21
22
23
24
25
26
27
28
29
30
31
32
33
34
35
36
37
38
39
40
41
42
43
44
45
46
47
48
49
50
51
52
53
54
55
56
57
58
59
60
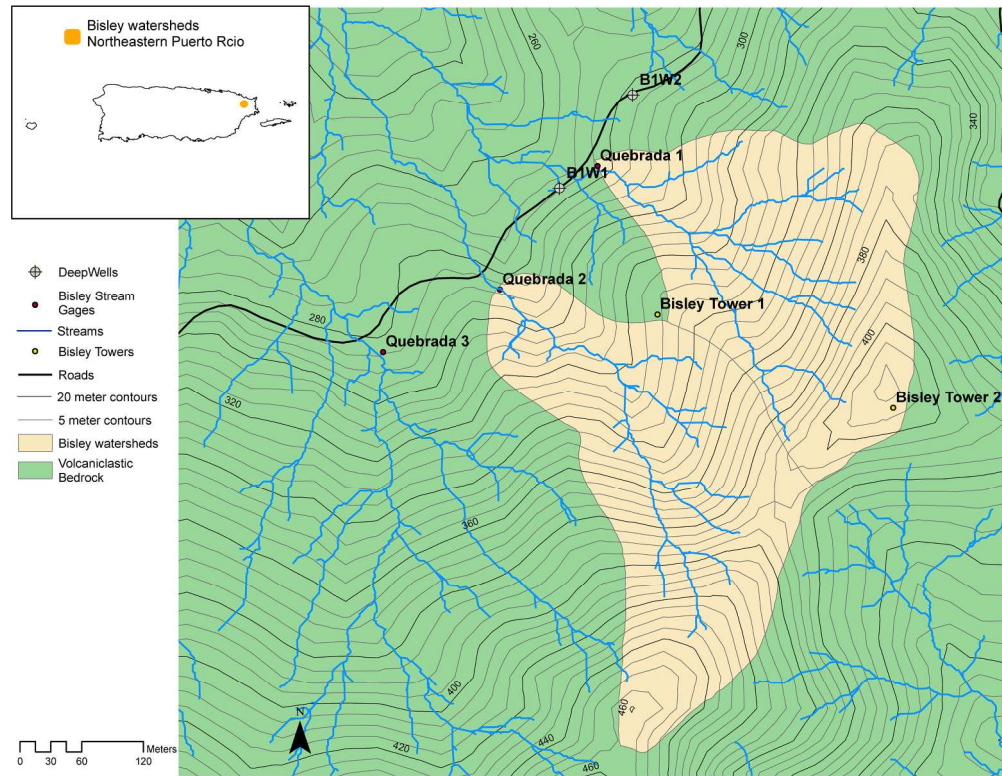
Figure 1. Map of volcaniclastic Bisley watersheds I and II. Quebradas I, II, and III are the Bisley streams. The two drilled boreholes are B1W1 and B1W2. (Figure supplied in color for online publication).
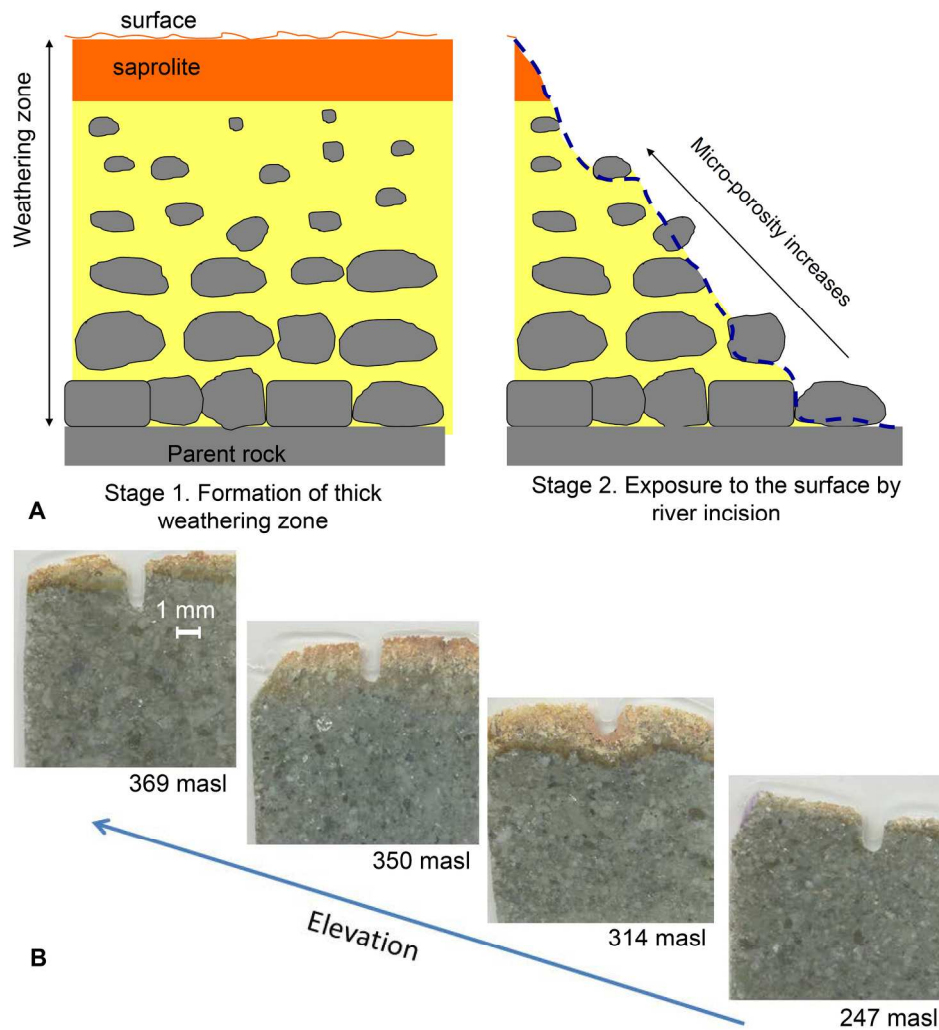215x166mm (300 x 300 DPI)

Figure 2. A. Simplified schematic view of a 100 m-thick weathering profile of in situ weathered bedrock blocks (corestones) underlying boulder-free saprolite, with the bedrock-corestone interface shown as horizontal. The first stage of critical zone development in the Bisley watershed is shown on the left, where corestones are shown schematically to decrease in size toward the land surface due to increased duration of weathering. The second stage of critical zone development is shown on the right, where corestones are exposed by a later episode of rapid erosion. B. Thick sections from corestones from different elevations in Bisley profile, Puerto-Rico. The outermost edge (top of the slides) shows the weathering rind development in cross-section. (Figure supplied in color for online publication).
201x213mm (300 x 300 DPI)

Figure 3. A plot of the profile of the Bisley I stream channel (after Fletcher and Brantley, 2010). Below ~220 masl, the Bisley I joins with the Bisley II and III tributaries. The combined stream joins the Rio Mameyes along a bedrock-lined channel just above 50 masl. Fletcher and Brantley (2010) observed that the maximum size of corestones did not vary below 200 masl, but decreased with increasing elevation above 200 masl. Below 200 masl, the slope of the Bisley channel is invariant until joining with the river at 50 masl. The plane of the channel between 50 and 200 masl was interpreted to be the plane across which corestones emerge from the fractured bedrock, or the saprolite-bedrock interface. If the weathering profile is roughly parallel to the bedrock-saprolite interface (as shown), the average weathering profile thickness is 135 m.
106x102mm (300 x 300 DPI)
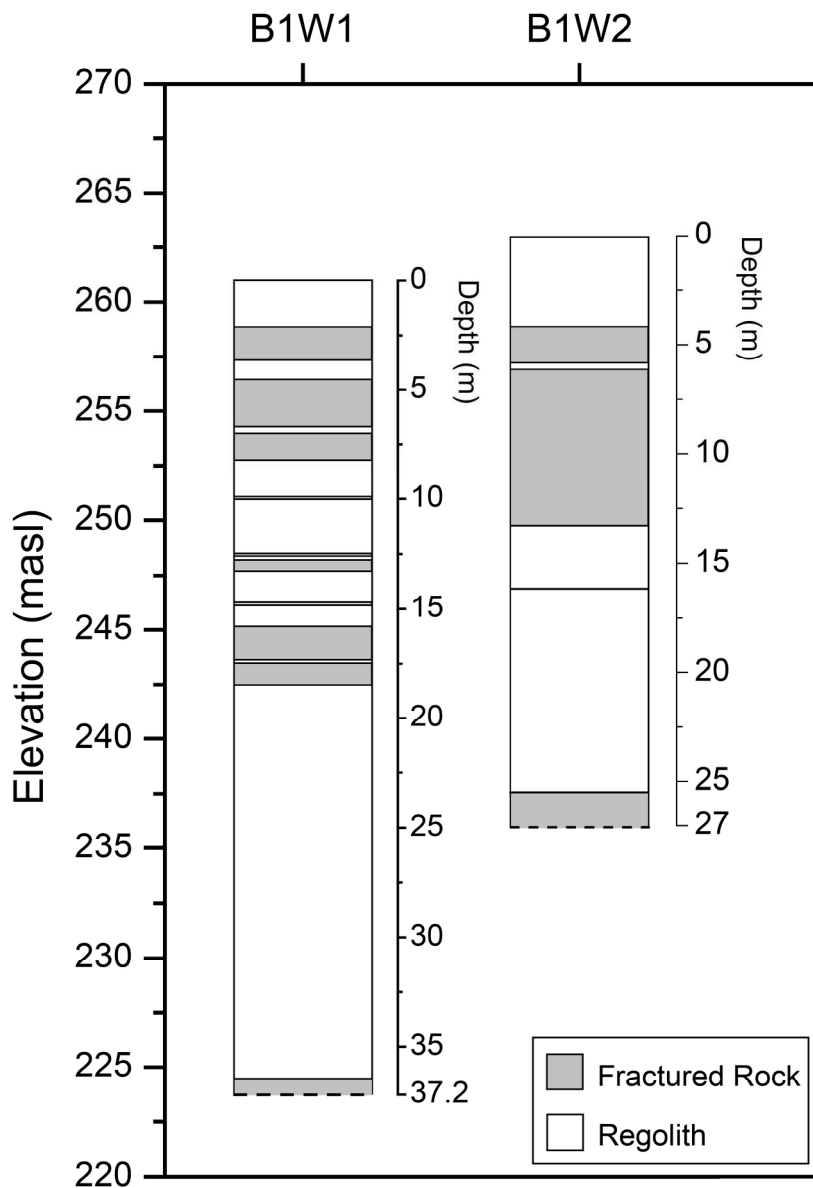
Figure 4. Diagram of boreholes drilled in the Bisley 1 watershed showing locations of recovered rock samples. Grey = fractured rock; white = granular material (i.e., saprolite or sediment). Regolith zones were mostly washed out during drilling without sampling although a few intact pieces of saprock were recovered. All rock recovered was highly fractured with fractures spaced at mms to cms. Dashed lines at bottom of the cores indicate the deepest extent of drilling into what is inferred here to be relatively un-weathered bedrock. 178x250mm (300 x 300 DPI)
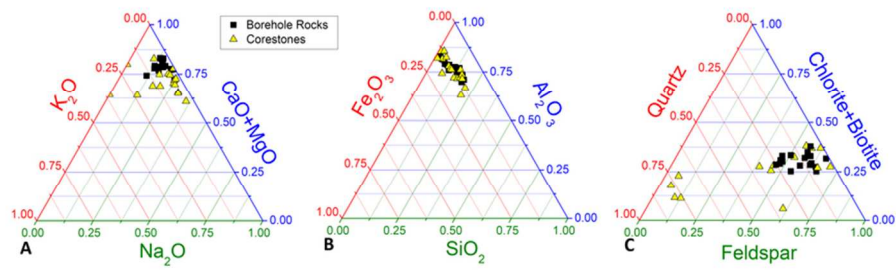
Figure 5. Ternary diagrams of Bisley rocks sampled from deep drilled boreholes or aboveground corestones. Data plotted here is for visibly un-weathered subsamples (weathered rinds were cut off before analysis). A) Borehole samples contain similar amounts of labile elements Ca, Mg, Na, and K, whereas corestone samples contain variable amounts of these elements indicative of weathering of some samples. B) Relative solid-state concentrations of total Fe, Al, and Si are similar in both borehole and corestone samples. C) High relative concentrations of quartz may be indicative of weathering in some of the corestone samples or evidence of hydrothermal alteration. (Figure supplied in color for online publication).
81x22mm (300 x 300 DPI)
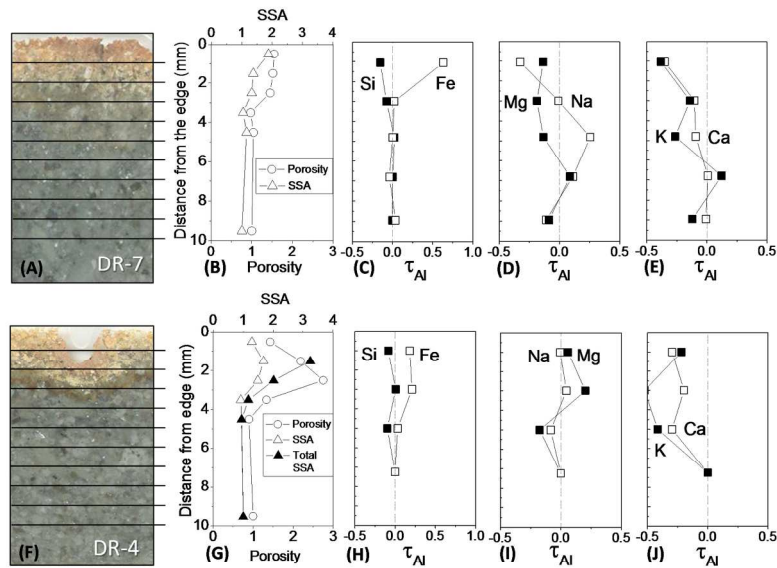
Figure 6. A-E) Data from corestone DR-7 (350 masl). F-J) Data from corestone DR-4. Vertical axis on all panels A-J is the distance from the outer edge of the weathered rind, in mm. (A, F) Photographs of thick sections with lines marking 1 mm spacing. (B, G) Changes in porosity and specific surface area (SSA) determined from neutron scattering data and normalized relative to the protolith (i.e., 9.5 mm). SSA (open triangles) determined from SANS data. Total SSA (closed triangles), measured only on DR-4 (314 masl), was determined from SANS+USANS data. Note that these methods are only capable of measuring scatterers smaller than ~10 μm , so "total" does not include porosity or SSA attributed to larger scatterers (e.g., pores > 10 μm). (C-E, H-J) Tau values for major elements were calculated from EDS data using Al as an immobile element. Parent composition was chosen as an average of the compositions measured at ~6-8 mm from the rind edge, which were assumed to represent un-weathered rock based on visual observation (Figure supplied in color for online publication).
209x148mm (300 x 300 DPI)

1
2
3
4
5
6
7
8
9
10
11
12
13
14
15
16
17
18
19
20
21
22
23
24
25
26
27
28
29
30
31
32
33
34
35
36
37
38
39
40
41
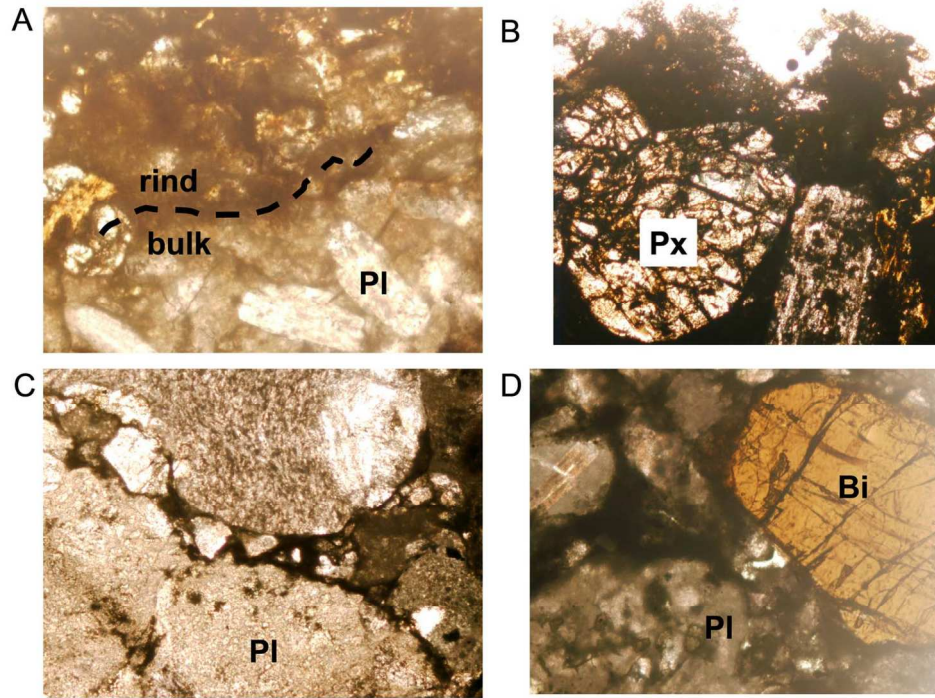42
43
44
45
46
47
48
49
50
51
52
53
54
55
56
57
58
59
60

Figure 7. Optical microscope images (20X magnification) of corestone sample DR-3, which consists mostly of anhedral large grains of plagioclase, smaller pyroxene grains, and occasional biotite grains. A) Weathering rind – bulk rock interface, B) The weathering rind contains fine-grained opaque minerals; large, a highly weathered pyroxene grain and small, white irregular grains, which may be disintegrating plagioclase. C) The bulk rock (10 mm inward from the weathering rind) contains patches of a brown-greenish stain within plagioclase and pyroxene grains and inter-grain cracks. D) Biotite grain and chlorite-stained plagioclase in the bulk rock (15 mm from the edge). Abbreviations: Pl – plagioclase; Px – pyroxene, Bi – biotite. (Figure supplied in color for online publication).
209x148mm (300 x 300 DPI)
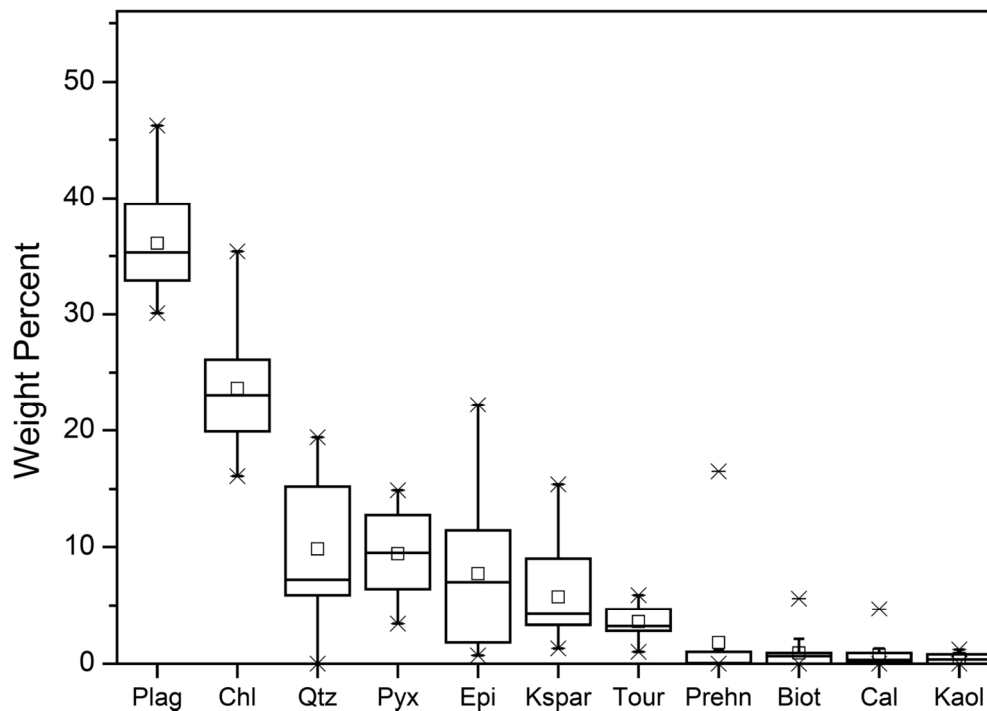
Figure 8. Box and whisker diagram showing mineral contents of 18 visibly un-weathered core samples from boreholes B1W1 and B1W2 as determined by quantitative XRD (Eberl, 2003). Wide boxes indicate 25-75% of data and are divided by a line denoting 50%. Small boxes indicate the mean, whiskers extend to outliers, X symbols indicate 1-99% of the data and small horizontal lines indicate maximum and minimum values. Mineral names are abbreviated as follows: Plag = plagioclase, Chl = chlorite, Qtz = quartz, Pyx = pyroxene, Epi = epidote, Kspar = K-feldspar, Tour = tourmaline, Prehn = prehnite, Biot = biotite, Cal = calcite, Kaol = kaolinite.
135x96mm (300 x 300 DPI)
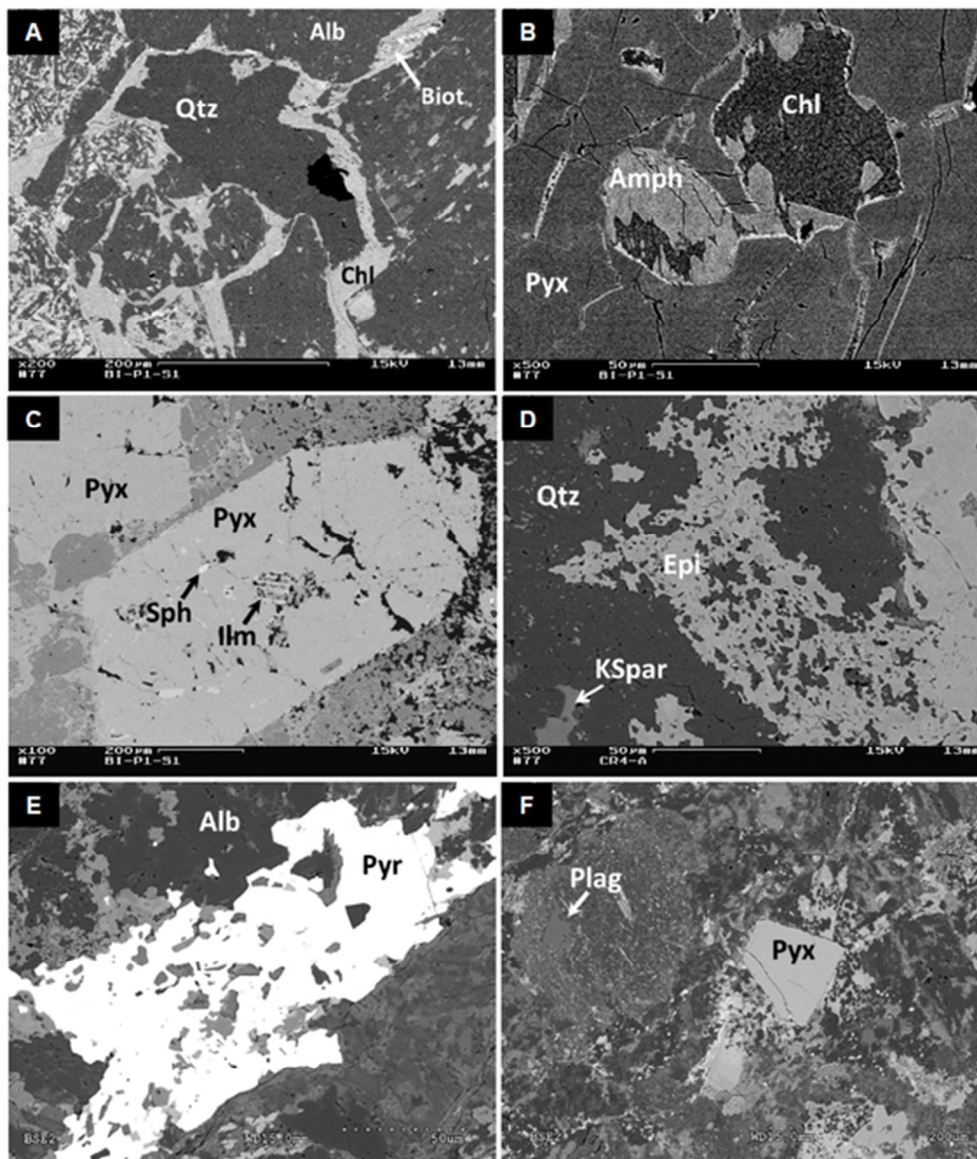
Figure 9. Backscattered SEM images of visibly un-weathered zones within a corestone rock sample from the Bisley 1 stream (A-C), a corestone exposed by a landslide (D), and core recovered from borehole B1W2 at ~8.4 m depth (E-F). A) Microcrystalline quartz (Qtz) and microcrystalline albite (Alb) are separated by a band of Fe, Mg chlorite (Chl). A biotite (Biot) crystal contains small inclusions of apatite. B) Amphibole (Amph) is visible embedded within clinopyroxene (Pyx), identified as augite. The interior of the amphibole crystals is altered to chlorite. C) Large pyroxene crystals are shown containing inclusions of titanite (sphene, Sph) and ilmenite (Ilm). D) Epidote (Epi) is distributed within microcrystalline quartz (Qtz). K-feldspar (KSpar) is also visible. E) Several zones of pyrite (Pyr) were found in this section of core. F) Crystals of calcic plagioclase (Plag) and pyroxene are shown surrounded by a groundmass of plagioclase, chlorite, titanite, and possibly other minerals. Images A-D were collected at the USGS in Menlo Park, CA. Images E-F were collected at the University of Bristol.
48x57mm (300 x 300 DPI)

1
2
3
4
5
6
7
8
9
10
11
12
13
14
15
16
17
18
19
20
21
22
23
24
25
26
27
28
29
30
31
32
33
34
35
36
37
38
39
40
41
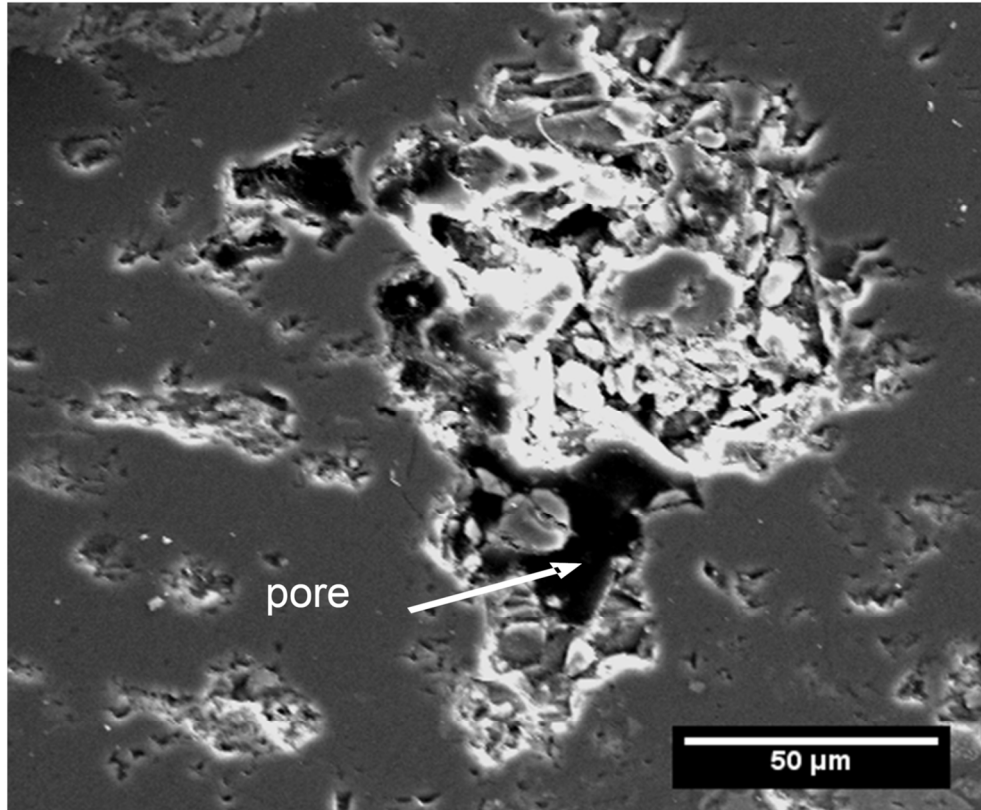42
43
44
45
46
47
48
49
50
51
52
53
54
55
56
57
58
59
60

Figure 10. Secondary Electron SEM image of corestone sample DR-7 taken 23 mm from the rind edge showing preferential porosity development within an epidote grain.
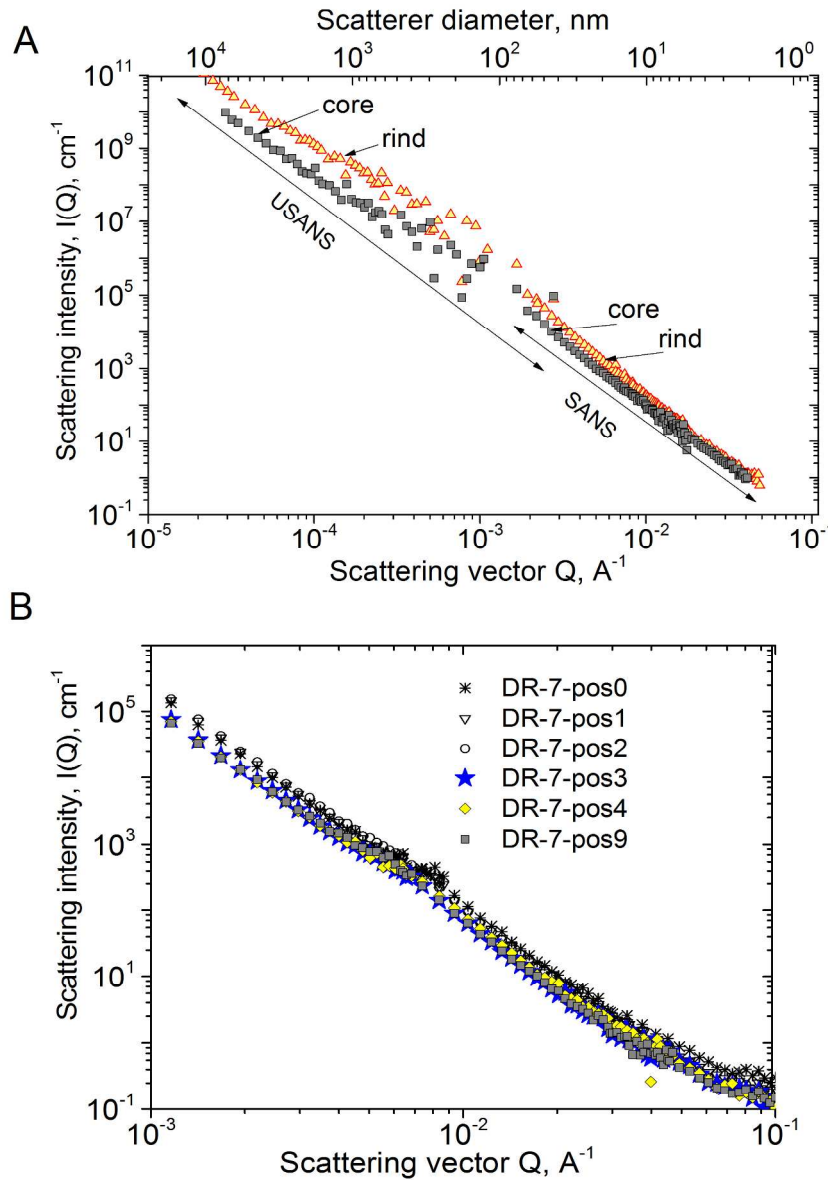123x101mm (300 x 300 DPI)

Figure 11. A) Neutron scattering data, I versus Q, for the rind (2.5 mm from the outer edge of the rind) and core (9.5 mm from the outer edge of the rind) of corestone sample DR-4. The rind has a higher scattering intensity due to higher porosity. Q regions for SANS and USANS and corresponding scatterer diameter (pore size) are also shown. B) SANS spectra for corestone sample DR-7, with distances in mm from the outer edge of the rind. The data from 9.5 mm represents the fresh rock. (Figure supplied in color for online publication) 205x271mm (300 x 300 DPI)
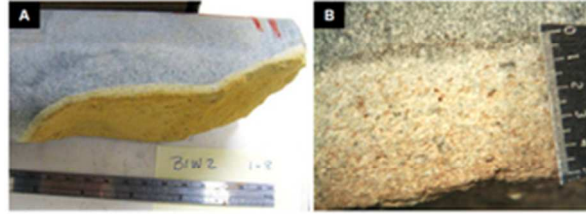
Figure 12. A) Photograph of a section of rock core from borehole B1W2 ~5.5 m below the ground surface. A weathering rind is visible along a natural fracture. B) Close up image of the rind shown in A. (Figure supplied in color for online publication).
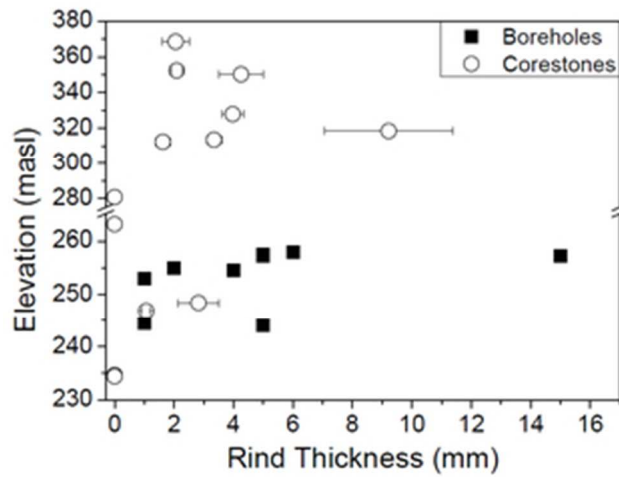25x15mm (300 x 300 DPI)

Figure 13. Rind thickness (mm) versus elevation (masl) for rock samples collected from exposed corestones and boreholes. Trends in rind thickness as a function of elevation are not apparent in either set of data, likely due to spalling off of thick rinds on exposed corestones at higher elevation. The R^2 is 0.12 for the borehole data, 0.42 for the corestone data (omitting the outlier), and 0.18 for the entire dataset (omitting the outliers).
26x20mm (300 x 300 DPI)